From the Department of Clinical Science,
Intervention and Technology (CLINTEC),
Division of Medical Imaging and Technology
Karolinska Institutet, Stockholm, Sweden

THERANOSTICS IN RADIOLOGY: DEVELOPMENT OF TARGETED CONTRAST MEDIA WITH TREATMENT CAPABILITY

Åsa Barrefelt

Stockholm 2014

All previously published papers were reproduced with permission from the publisher.

To my Family ♥

Någonstans finns det något fantastiskt som väntar på att bli upptäckt
Somewhere, something incredible is waiting to be known - Carl Sagan

ABSTRACT

Imaging is essential in the diagnostics and medicine of today. The development of new contrast agents is important for obtaining specific information from images and to distinguish disease. Microbubbles (MB) have previously been introduced as a contrast agent for ultrasound. By incorporating super paramagnetic iron oxide nanoparticles (SPION) to the polymer matrix of the MB or between its shell layers we obtain a contrast media for Magnetic Resonance Imaging (MRI); while functionalizing the MB by ligands for labeling with [99mTc] enables imaging using Single-Photon Emission Tomography (SPECT). The use of hybrid SPECT- and Computed Tomography (CT) or MRI systems enables fusion of the images from the different modalities to obtain SPECT/CT or SPECT/MR images. In the research underlying this thesis we investigated the preclinical characteristics, biodistribution and kinetics of several types of MB in Sprague Dawley rats by injecting single- and multiple layer SPION MB as well as ligand functionalized- and SPION MB labeled with [99mTc]. The results obtained from imaging was correlated and compared to the histopathology of MB findings in organs. Moreover, mice were injected with Alexa-680 Vivo Tag labeled MB for imaging using a pre-clinical In Vivo Imaging System (IVIS)/μCT.

Sprague Dawley rats (300 ± 50 g) were injected with single layer SPION-, multiple layer SPION-, [99mTc]-labeled ligand functionalized diethylenetriamine penta-acetic acid (DTPA)-, thiolated poly(methacrylic acid) (PMAA)-, chitosan-, 1,4,7-triazacyclononane-1,4,7-triacetic acid (NOTA)-, NOTA-SPION- or DTPA-SPION MB *intravenously* (*i.v.*) through the tail vein. The rats injected with SPION MB were scanned using MRI, while the rats injected with [99mTc]-labeled DTPA-, PMAA-, chitosan- or NOTA MB were scanned using SPECT/CT. The rats injected with NOTA-SPION- or DTPA-SPION MB were co-registrated using SPECT/CT and MRI. The organs from rats injected with the nuclear medicine marker were removed *post mortem* and measured for radioactivity. The rats injected with SPION MB were sacrificed and their organs were removed *post mortem* for histopathology examination using Perls' Prussian blue staining to show iron content and immunohistochemistry (IHC) to visualize macrophage uptake of MB.
Mice (30 ± 5 g) were injected with multiple layer fluorescence Alexa-680 MB and imaged using IVIS. Their organs were removed *post mortem* and examined using pathology and the fluorescence of MB was visualized under the microscope.

The uptake of MB was mainly seen in the lungs and liver 1-2 h post-injection, while the main distribution of MB at 24 h post-injection was seen in the liver. In conclusion the MB matrix can be functionalized by ligands, labeled by SPION, [99mTc] and fluorescence Alexa-680 Vivo Tag to enable its visualization *in vivo* using multimodal imaging SPECT/CT, SPECT/MRI or IVIS/μCT. Furthermore we have shown that MB can be loaded with cytostatic- or inflammatory drugs for theranostics. Future studies regarding MB should address toxicity and efficiency in drug loading and delivery.

LIST OF PUBLICATIONS

I.   Brismar B. Torkel, Grishenkov Dimitry, Gustafsson Björn, Härmark Johan, **BARREFELT ÅSA**, Kothapalli V.V.N. Satya, Margheritelli Silvia, Oddo Letizia, Caidahl Kenneth, Hebert Hans, Paradossi Gaio. *Magnetite Nanoparticles Can Be Coupled with Microbubbles to Support Multimodal Imaging*. Biomacromolecules 2012 May 14;13(5):1390-9, Copyright © 2012 American Chemical Society. DOI: 10.1021/bm300099f, PMID: 22458325.

II.   **BARREFELT ÅSA**, Paradossi Gaio, Asem Heba, Margheritelli Silvia, Saghafian Maryam, Oddo Letizia, Muhammed Mamoun, Aspelin Peter, Hassan Moustapha[*] and Brismar B. Torkel[*]. *Dynamic MR imaging, Biodistribution and Pharmacokinetics of Polymer-Shelled Microbubbles containing SPION*. Submitted manuscript.

III.   **BARREFELT ÅSA**, Brismar B. Torkel, Egri Gabriella, Aspelin Peter, Olsson Annie, Oddo Letizia, Margheritelli Silvia, Caidahl Kenneth, Paradossi Gaio, Dähne Lars, Axelsson Rimma[*], Hassan Moustapha[*]. *Multimodality imaging using SPECT/CT and MRI and ligand functionalized 99mTc-labeled magnetic microbubbles*. EJNMMI Research 2013, Feb 25; 3(1):12. © 2013 Barrefelt et al; licensee Springer. DOI: 10.1186/2191-219X-3-12, PMID: 23442550.

IV.   **BARREFELT ÅSA***, Saghafian Maryam*, Kuiper Raoul, Ye Fei, Egri Gabriella, Klickermann Moritz, Brismar B. Torkel, Aspelin Peter, Muhammed Mamoun, Dähne Lars, Hassan Moustapha. Biodistribution, Kinetics and Biological Fate of SPION Microbubbles in the Rat. International Journal of Nanomedicine 2013:8(1) Pages 3241-3254, © 2013 Barrefelt et al. Published by Dove Medical Press Ltd. DOI: 10.2147/IJN.S49948, PMID: 24023513.

V.   **BARREFELT Å.**, Larsson K. M.[*], Zhao Y.[*], Egri G., Kuiper V. R., Hamm J., Saghafian M., Caidahl K., Brismar B. T., Aspelin P., Heuchel R., Muhammed M., Dähne L., Hassan M.. *Multimodal Imaging of Fluorescence Labeled Microbubbles*. Manuscript.

Other work, not included:

VI.   El-Sayed Ramy, Eita Mohamed, **BARREFELT ÅSA**, Ye Fei, Jain Himanshu, Fares Mona, Lundin Arne, Crona Mikael, Abu-Salah Khalid, Muhammed Mamoun, Hassan Moustapha. *Thermostable Luciferase from Luciola cruciate for Imaging of Carbon Nanotubes and Carbon Nanotubes Carrying Doxorubicin Using in Vivo Imaging System*. Nano Letters, 2013, 13 (4), pp 1393-8. Copyright © 2013 American Chemical Society, DOI: 10.1021/nl304123u. PMID: 23520995.

VII.   Ye Fei, **BARREFELT ÅSA***, Asem Heba*, Abedi-Valugerdi Manuchehr; El-Serafi Ibrahim, Saghafian Maryam, Abu-Salah Khalid, Alrokayan Salman, Muhammed Mamoun, Hassan Moustapha. *Biodegradable Polymeric Vesicles Containing Magnetic Nanoparticles, Quantum Dots and Anticancer Drugs for Drug Delivery and Imaging*. Biomaterials. 2014, Feb 1. pii: S0142-9612(14)00057-X, Copyright © 2014 Elsevier Ltd. http://dx.doi.org/10.1016/j.biomaterials.2014.01.041, PMID: 24495486.

CONTENTS

LIST OF ABBREVIATIONS

2D	Two-dimensional
3D	Three-dimensional
AG	Aminoguanidine
AUC	Area under curve
Bu	Busulfan
C_{max}	Maximum concentration
CT	Computed Tomography
DTPA	Diethylenetriamine penta-acetic acid
FID	Free induction decay
FITC	Fluorescein isothiocyanate
GRE	Gradient echo
I.V.	*Intra venous*
ICAM	Intracellular Adhesion Molecule
IHC	Immunohistochemistry
IVIS	*In Vivo* Imaging System
LbL	Layer by Layer
LPS	Lipopolysacharides
M	Net magnetization vector
MB	Microbubbles
MRI	Magnetic Resonance Imaging
M_{XY}	Transverse magnetization
M_z	Longitudinal magnetization
NMR	Nuclear magnetic resonance
NOTA	1,4,7-triazacyclononane-1,4,7-triacetic acid
PAH	Poly(allyl) amine hydrochloride
PEI	Poly(ethylene) imine
PET	Positron Emission Tomography
PLGA	Poly(lactic-co-glycolic acid)
PMAA	Poly(methacrylic) acid
PSS	Poly(styrene)sulfonat
PVA	Poly(vinyl) alcohol
R2*	Relaxation rate
RES	Reticuloendothelial system
RF	Radio frequency
ROI	Region of interest
SPECT	Single-Photon Emission Computed Tomography
SPION	Superparamagnetic iron oxide nanoparticles
SPR	Surface plasmon resonance
T1	Spin-lattice/longitudinal relaxation time
T2	Spin-spin/transverse relaxation time
T2*	Rate of decay of phase coherence
T	Tesla

TE	Echo time
TEM	Transmission electron microscopy
TIRM	Turbo Inversion Recovery Magnitude
T_{max}	Time to reach C_{max}
TR	Repetition time
V-CAM	Vascular Cell Adhesion Molecule
B_0	The external magnetic field of the MR scanner
β_0	Static magnetic field
λ	Gyromagnetic ratio
ω_0	Larmour frequency

1 INTRODUCTION

1.1 BACKGROUND

Imaging is essential in diagnostics today. The combination of imaging modalities to get the most relevant characteristics from each modality is of great interest for future clinical applications. Combining dual or triple imaging methods with short time and space lapse in hybrid systems supports the growing interest in *in vivo* multimodal- and targeted imaging. Furthermore, contrast agents can improve the distinction and identification of different tissues and pathologic structures since they provide an increase, such as a positive contrast, or decrease, such as a negative contrast, in images [1-3]. There is no contrast agent for combined imaging available today. Thus, exams using different modalities are normally carried out on different days, which might prolong the time it takes to obtain a diagnosis by several weeks. The development of multimodal contrast agents could enable exams to be carried out during a single day, which would be beneficial to the individual patient as well as to the health care system by shortening the time to diagnosis as well as leaving more beds and equipment free for other patients [4-8]. When developing a new contrast agent, it is important to determine its pharmacokinetic properties and to investigate its biodistribution over time in animal models before testing the substance in humans [9-16]. In the current thesis we investigate a potential new delivery system of a tri-modality-suited contrast agent consisting of polymer shelled, poly(vinyl) alcohol microbubbles (MB).The polymer matrix has an amazing property in that it can be functionalized with several ligands [17], i.e. diethylenetriamine penta-acetic acid (DTPA), 1,4,7-triazacyclononane-1,4,7-triacetic acid (NOTA), poly(methacrylic) acid (PMAA) and chitosan to bind ^{99m}Tc, a radiotracer which enables the MB to be visualized using Single-Photon Emission Computed Tomography (SPECT) [18]. Moreover, the MB can be incorporated with nanoparticles such as superparamagnetic iron oxide nanoparticles (SPION), either physically bound inside the shell, chemically bound to the MB PVA matrix using covalent bonding or trapped in between the layers of the MB shells [19]. SPION enables the magnetic SPION MB to be used as a contrast agent for magnetic resonance imaging (MRI) [20, 21]. MRI is a non-invasive, high resolution diagnostic method that provides information on morphological and physiological changes of internal organs over time. Imaging and measurements can be repeated on the same subject, thereby reducing inter-variability effects and hence the number of subjects required in a study. This in turn saves time and money as well as animals, according to the three R:s, Replace, Reduce and Refine. The capacity of the MB system for the functionalization of multiple nanoparticles and/or ligands enables its use as a multimodal imaging agent by visualizing both function and anatomy in one image using hybrid SPECT/Computed tomography (CT) or SPECT/MR systems. Pre-clinical studies are warranted in the development of new contrast agents before reaching the clinical phase in pharmaceutical development, and several animal studies are necessary before trying the substance in humans. The development of pharmaceuticals moves from an exploratory/preclinical phase in animals to human I-IV studies. The exploratory phase

include pharmacokinetics-, safety- and toxicity studies of the pharmaceutical in mice, rats and larger animals such as pigs before reaching the clinical phase [22-25].

The present studies were carried out in the preclinical phase in rats and mice. Ligand functionalized- and SPION MB were injected *intravenously* (i.v.) into Sprague Dawley (SD) rats to determine their biodistribution, biological fate and pharmacokinetics using fusion SPECT/CT/MR imaging. Moreover, the I*n Vivo* Imaging System (IVIS) can be used in combination with MRI or CT to visualize the biodistribution of fluorescence MB such as Alexa-680 Vivo Tag labeled MB (Alexa-680 MB). In recent years, nanoparticles and micro vehicles such as microbubbles have become interesting targets for multimodal imaging and drug delivery. The MB and the developed imaging methods and protocols have a future potential for use in the imaging of tumors and cancers, in diagnostics and for inflammatory models. In my PhD thesis I have studied a potentially new, multifunctional contrast agent supporting multimodal imaging using MRI with a high spatial resolution, SPECT for quantitative imaging, CT for anatomy and IVIS for the preclinical work. The organ biodistribution obtained using multimodal imaging techniques was verified in the organs by histopathology and by the measurement of radioactivity in the respective organs *post mortem*.

1.2 MAGNETIC RESONANCE IMAGING

Magnetic resonance imaging (MRI) is considered state of the art in diagnostics and was originally used for imaging of lesions and pathologic structures since it has a high resolution for soft tissue. In contrast to CT, SPECT and PET, MR imaging requires no iodinated or radioactive contrast agents. MRI is free of biological hazardous materials and is a non-invasive technique. Due to its high spatial resolution, it was originally used mainly for brain imaging [26]. Originally, Raymond Damadian proposed nuclear magnetic resonance (NMR) scanning of patients to obtain a diagnosis [27]. He proposed that cancer and normal tissue can be distinguished using MRI, due to their different relaxivities [28, 29]. Damadian was followed by Paul Lauterbur, who published a new imaging method that was called Zeugmatography. This new technique generated the first 2D- and 3D MR images moving the application of NMR spectroscopy from a single dimension to a second dimension of spatial orientation. That became the foundation of today's MRI technology [30-32]. Peter Mansfield, who later was awarded the Nobel Prize in medicine together with Paul Lauterbur, developed a mathematical technique that would allow scans to take seconds rather than hours. This technique also produced clearer images. NMR is the basis of MRI which involves the interaction between a static magnetic field and protons that align perpendicular to the magnetic field (ß0). In the MR scanner there are also three gradient magnets responsible for the ability of MRI to create "slices" of the body in the MR tomography. The nuclei of the hydrogen (H) atoms spin in one of two directions. By exposure of the external, static magnetic field of the MR scanner, β_0, the spin of the nucleus takes one of two directions, anti-parallel or parallel. The difference of the vectors, the net magnetization vector M, is parallel to the static magnetic field.
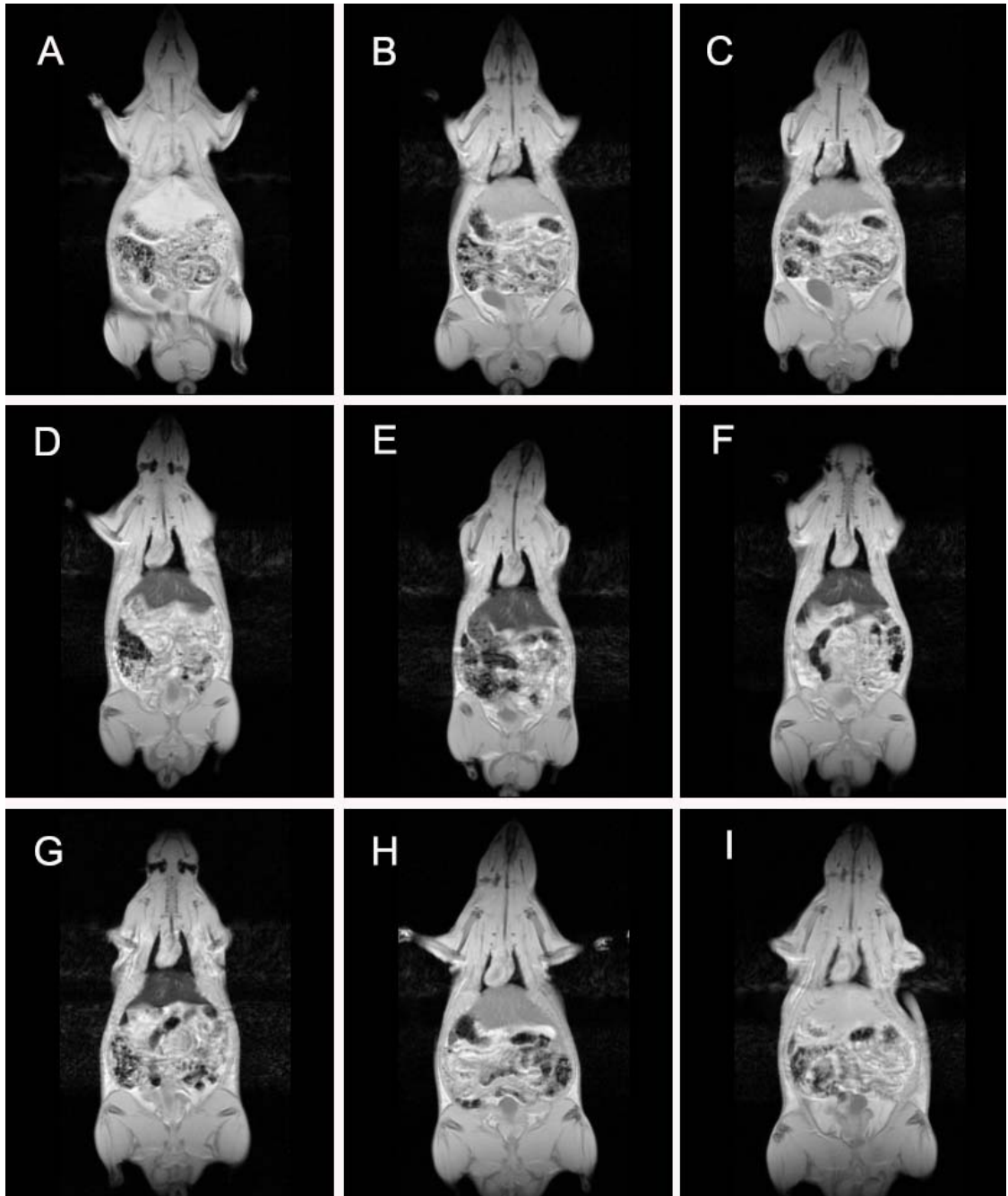
Figure 1. A Sprague Dawley rat (300 g) imaged prone using an in-house developed T2* sequence at 3 T (Siemens Trio, Siemens, Erlangen, Germany). MR signal intensity changed mostly in the liver over time from 10 min to 6 weeks compared to pre-injection. (A) pre-injection, (B) 10 min, (C) 1 h, (D) 24 h, (E) 48 h, (F) 1 week, (G) 2 weeks, (H) 4 weeks and (I) 6 weeks post-injection. Published by Barrefelt et. al. in International Journal of Nanomedicine 2013:8(1) pages 3241 – 3254.

When applying a radiofrequency (RF) using the coil, a transition takes place exactly at the Larmour frequency, $\omega_0 = 42.58$ MHz/Tesla:

$\omega_0 = \lambda\beta_0$ (where $\lambda = 42.57$ MHzT^{-1})

This will transfer energy to the precessing protons [33]. By turning off the RF pulse the excited nuclei return to their initial equilibrium state. The process of relaxation then generates a MR signal picked up by the receiver coils. The magnitude of this vector is an exponential function of time, the free induction decay (FID). The processes are recorded and reconstituted by the MR scanner to obtain gray scale images.

The relaxation involves both T1 and T2 relaxation. T1 is the longitudinal relaxation from the excited state to the surrounding, denoted spin lattice relaxation time; which reflects nuclei falling back from the high to the low energy state and is the time for 63 % recovery of a decreased longitudinal net magnetization (M_z). T2 (spin-spin relaxation) reflects the decay of transverse magnetization (M_{xy}) from the induced disappearance of transverse magnetization to the perpendicular plane (M_{xy}) by the dephasing of the spins. T2 is the decay of 37 % of the signal. T2 arises from the exchange of energy between spins wherein no energy is lost from the spin system, but the decay of magnetization arises from the loss of phase coherence of the precessing nuclei. 1/T2 is the transverse relaxation rate.

The dephasing is eliminated by applying a 180 degree pulse. However, in gradient echo sequences there is no 180 degree refocusing pulse and the dephasing effects are not eliminated, which is why transverse relaxation in gradient echo (GRE) sequences is a combination of T2 relaxation and by the relaxation caused by magnetic field inhomogeneities caused by the air filled microbubble as in:

1/T2* = 1/T2 + $\lambda\Lambda$B or 1/T2* = 1/T2 + 1/T2'

T2* is the rate of decay of phase coherence or decay of transverse magnetization and heterogeneities of the environment. T2* is faster than T2 due the inhomogeneity in the magnetic field. Furthermore, magnetic field inhomogeneities are either macroscopic and include deoxyhemoglobin in tiny veins, metallic implants, or microscopic such as paramagnetic contrast agents, blood or iron deposits or air tissue interaction such as in air filled MB [34]. Dephasing areas, lesions or structures are shown as dark areas on T2* weighted images. T2* decay starts with excitation and progression within time, and the longer the echo time (TE) the greater the signal loss because of more dephasing, a low flip angle, long TE and long TR. T2* weighted imaging is commonly used for MR perfusion or MR functional imaging. The loss of RF signal means loss of phase coherence, so called "dephasing", which comes from the loss of spin-spin relaxation expressed by T2. This can be cancelled by a spin-echo maneuver in which a 90º RF pulse is applied and serves to re-gather the transverse relaxation vectors to emit a strong signal [35]. In fluids, the T2 and T2* times will be longer and signal intensity lower, whereas in water based tissues such as muscle and fat they will be of

intermediate intensity. With shorter TEs, fluids lose their brightness. T2 is often called pathology scans.

By injecting a rat by SPION MB and imaging it dynamically at different time points (Figure 1) we can calculate the concentration of SPION MB in the respective organs. By using several TE:s and measuring the signal intensity, with the least possible standard deviation, in a region of interest (ROI) on T2* weighted MR images and plotting the signal intensity towards the respective TE value we obtain graphs (Figure 2). By plotting the logarithmic value of the signal intensities versus the TE values we obtain a straight line for each time point (Figure 3). The spin-spin relaxation time, T2 star (T2*) is thus calculated as the negative slope of a semi-log plot of the signal intensities versus the TE:s. The slopes describes R2* (1/T2*), the relaxation rate, the amount of iron oxide at each time point. T2* or R2* can be calculated in agarose phantoms of known iron oxide concentrations and plotted to obtain a standard curve. R2* in rat liver (Figure 4) can then be correlated to the concentration, using the standard curve, and plotted versus time. Furthermore, pharmacokinetic calculations will enable the estimation of half-life, clearance, C_{max}, T_{max} and AUC of SPION MB by using MR imaging.
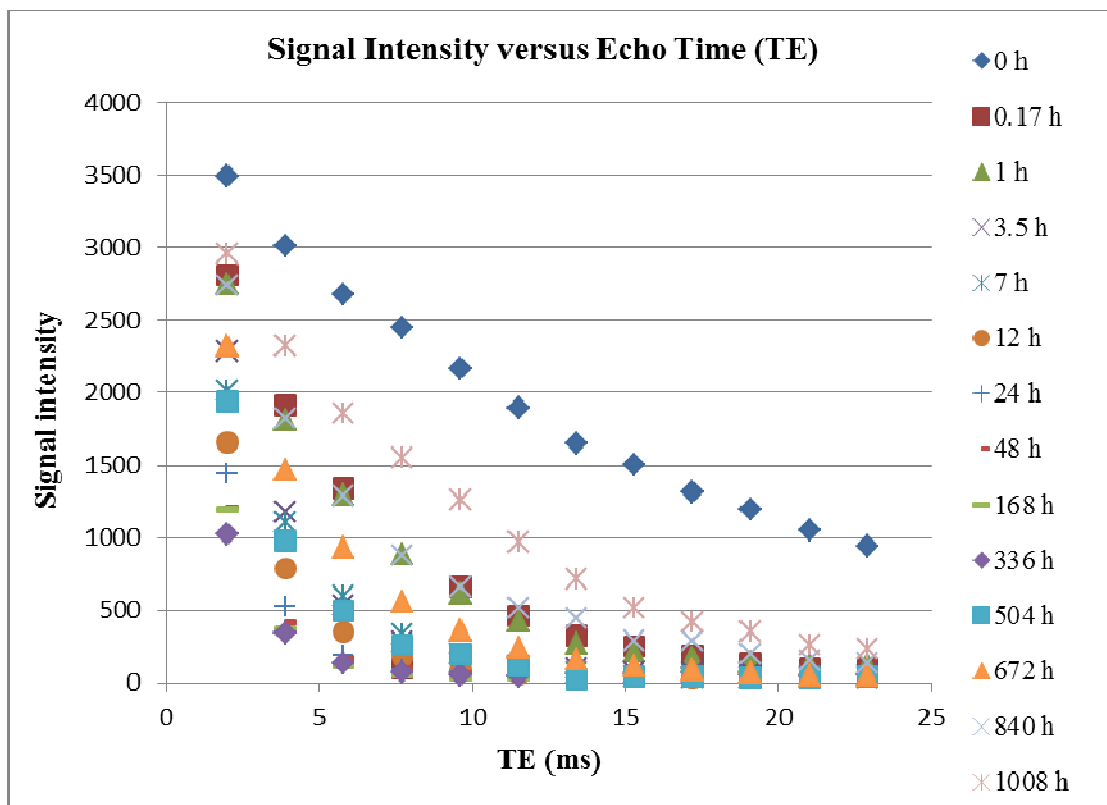
Figure 2. Signal intensity versus TE pre- and post-injection of SPION MB in rat. The graph shows that by an increase of iron oxide in the tissue by time, a greater signal loss is obtained.
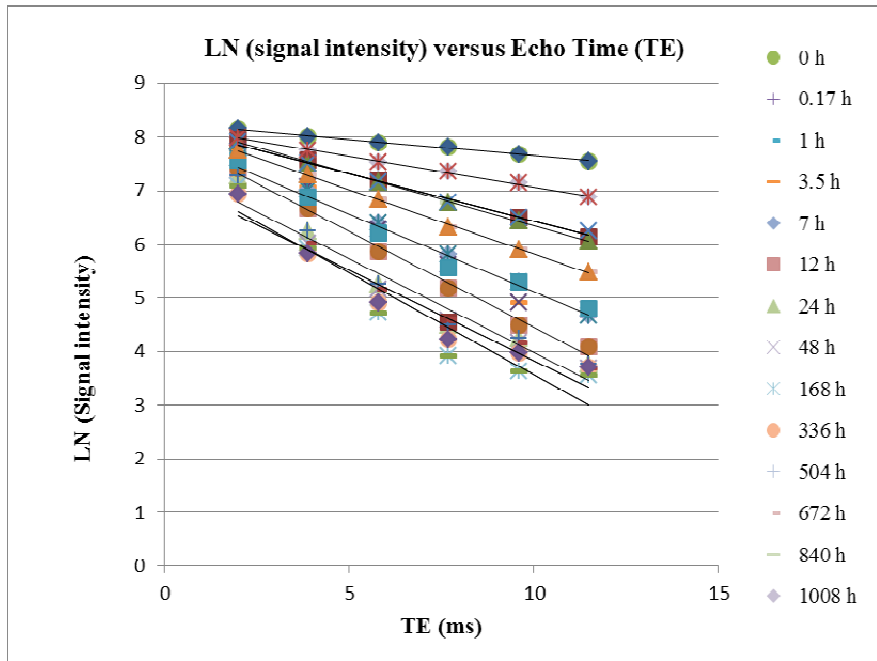
Figure 3. T2* is calculated as the negative slope of the semi-log plot of the signal intensities versus the TE values. The slopes describes R2* (1/T2*), which is the amount of iron oxide in the liver tissue of a rat at different time points pre- and post-injection of SPION MB
.
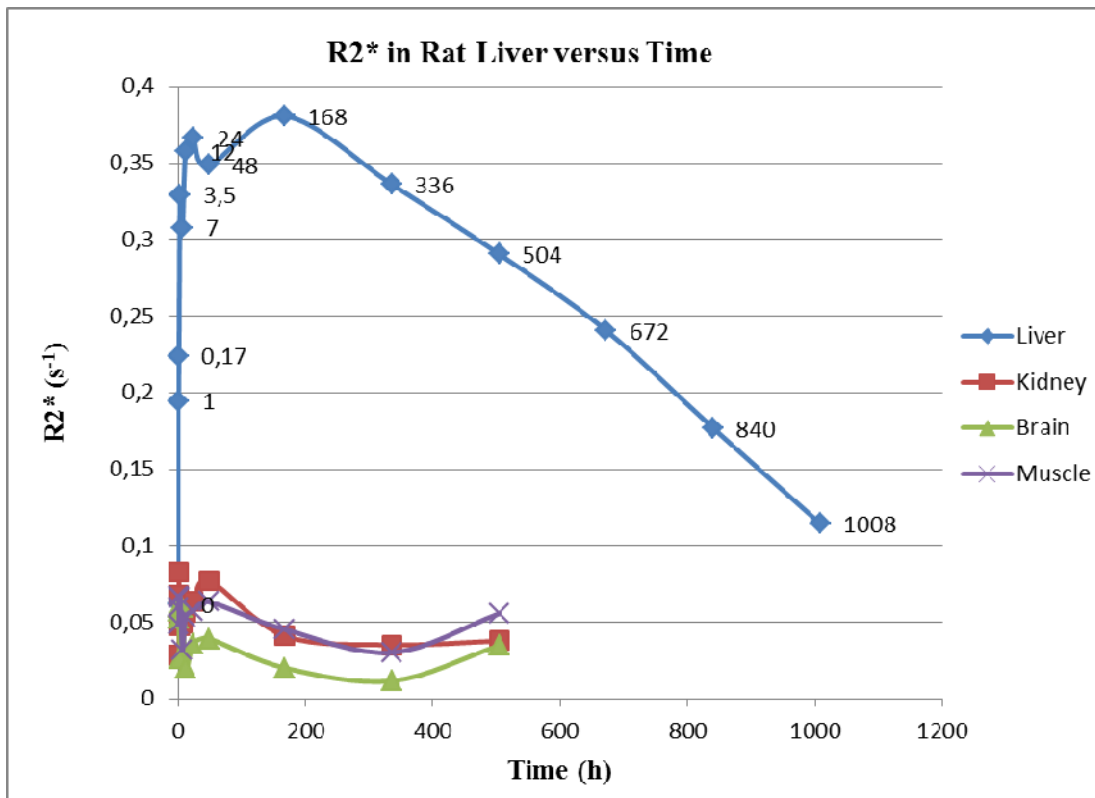
Figure 4. Dynamic 3 T MR imaging (Siemens Trio, Siemens, Erlangen, Germany) of R2* (s^{-1}) versus time (h) in rat liver (blue), pre- and post-injection of multiple layer SPION MB. ROI measurements and calculated R2* in kidney (red), brain (green) or muscle (lilac) shows no significant uptake of SPION MB.

6

1.3   X-RAY COMPUTED TOMOGRAPHY

A new era in medicine was introduced when Wilhelm Röntgen captured the first X-ray images of his wife's hand in 1895 [36]. X-ray computed tomography (CT) has since been intensively used in many applications such as fusion imaging in combination with SPECT or positron emission tomography (PET) imaging. CT provides anatomical information which can be overlaid on functional images to aid in the interpretation of organ uptake of radiotracer in nuclear medicine images. The CT technique is based on the fact that different tissues have different levels of X-ray absorption, which generates diverse contrast intensities on images. Tissues that differ as little as 1 % from each other in physical density can be distinguished on CT images. Barium or iodine contrast agents are used clinically for the detection of contrast on CT images. Hounsfield units (HU) is the scale for radiodensity. Furthermore, exciting future developments could be possible in the use of new CT contrast agents such as Gold (Au) nanoparticles, utilizing the property of Surface Plasmon Resonance (SPR). Au can be attached to polymers and MB and has been shown to have better contrast properties than commercial CT contrast agents [37]. This is an exciting and emerging field yet to be further explored.

1.4   NUCLEAR MEDICINE IMAGING

1.4.1   Dynamic Planar Scintigraphy

Scintillation cameras/gamma cameras consist of a collimator, two detectors made of NaI (3.67 g/cm3) crystals (33x43 and 37x59 cm) with thicknesses between 0.64 and 1.9 cm); which efficiently produce light photons (one photon per approximately 30 keV) upon interaction with γ-rays in the presence of Thallium (T1), positioning circuit. Photomultiplier (PM) tubes consisting of a light-sensitive photocathode at one end, metallic electrodes in the middle and an anode at the other end, pre-amplifiers and linear amplifiers, PHA and display [38]. The scintillation camera, Symbia True Point 16 hybrid system, Siemens, Erlangen, Germany, used in this thesis consist of a parallel hole collimator enabling high-resolution and high-sensitivity imaging with the highest resolution at the collimator face. Dynamic planar scintigraphy can be used to follow the uptake of a gamma-emitting heavy radioisotope/radioactive tracer such as ^{99m}Tc, ^{123}I, ^{67}Ga and ^{111}In over time. It can be visualized on dynamic gamma camera graphs, where the number of counts (Cnt) as measured in circular regions of interest (ROIs), placed in the organs on images, are plotted versus time (min). Anger developed the first clinically used scintillation camera to use PMT tubes for the detection of exactly where the flash of light occurs [39, 40].

1.4.2   Single-Photon Emission Computed Tomography

Tomography images are obtained by imaging the patient from different angles such as anterior, posterior and lateral, and by applying rigorous mathematical algorithms to reconstruct the images. The SPECT system utilized in this thesis consists of a gamma camera with two heads mounted on a gantry and on-line computers for acquisition and data processing. The detector heads rotate around the long axis of the patients in small angle increments for a total of 360°. The data is stored in 128 x 128 matrices for the

reconstruction of transverse, sagittal and coronal images. The limitation of scintillation cameras is that they depict images of three-dimensional activity in two-dimensional displays [41].

1.5 FUSION IMAGING: SPECT/CT, SPECT/MRI, IVIS/µCT OR IVIS/MRI

Hybrid imaging is carried out using several modalities, combining the images by fusion imaging to obtain SPECT/CT, SPECT/MR, IVIS/CT or IVIS/MR images. Fusion imaging can localize lesions, tumors or uptake of radioactive- or fluorescent tracer injected into the patient or animal [18, 42, 43]. The CT and MR images give anatomical information providing an organ atlas and structural information, whereas the SPECT and image gives functional information and characterizes functional abnormalities [44]. Fusion imaging is also helpful when using IVIS in preclinical studies to show the uptake location and biodistribution of fluorescent probes [43, 45]. The IVIS image is fused with an image acquired using µCT.

1.5.1 ^{99m}Tc as a Radioactive Tracer

^{99m}Tc is the most commonly used clinical radiopharmaceutical [46-51]. It has favorable characteristics with a relatively short half-life of 6 h and a small amount of electron emission with a minor radiation dose to the patient. The monochromatic 140 keV photons are easily collimated, resulting in images with a high spatial resolution to the patient. When eluted from the generator ^{99m}Tc has oxidation state +VII, which is why reduction to a lower oxidation state is required before labeling any other compounds. Stannous chloride (SnCl$_2$·2H$_2$O), dithionite or ferrous sulfates are some examples of reducing agents. After reduction, ^{99m}Tc is chemically reactive with various chelating compounds, donating electrons to form co-ordination bonds with the reduced ^{99m}Tc carboxyl- (-COO$^-$), hydroxyl (-OH$^-$), amine- (-NH$_2$) or thiol (-SH) groups existing in chelating agents. ^{99m}Tc labeled compounds are thereafter injected into animals or patients, where they emit photons that can be imaged using gamma camera and SPECT [18, 52]. In this thesis I used ^{99m}Tc labeled MB, imaging their uptake and biodistribution using SPECT for anatomy, and co-registrationd to get fusion SPECT/CT and SPECT/MR images which can localize the organ or region of uptake and visualize biodistribution [18].

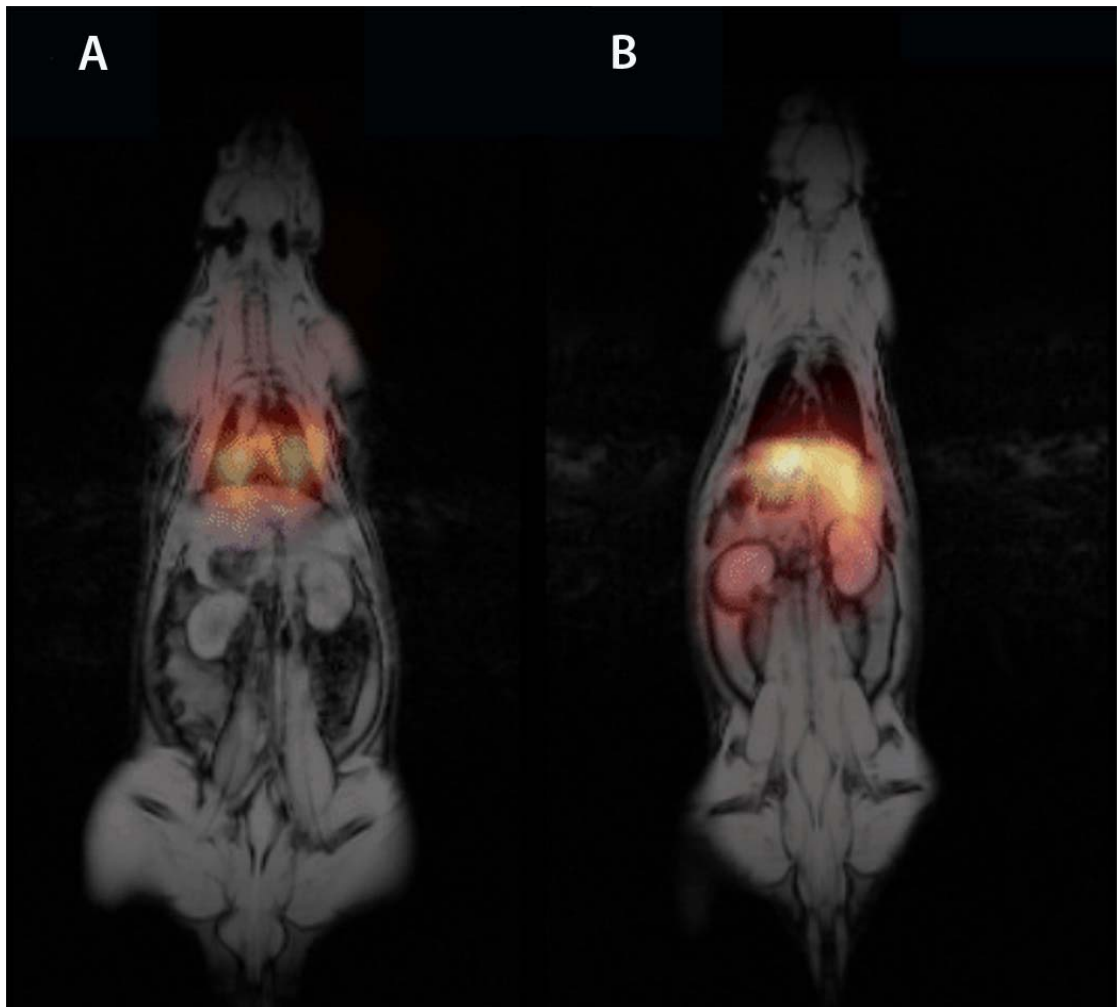**Figure 5.** Multimodal imaging using fusion SPECT/MRI. SPECT enables the functional visualization of MB in the lungs 1 h post-injection (A) and in the liver and kidneys 24 h post-injection (B); while MRI enables the visualization of an anatomical image of the rat and visualizes SPION MB in the liver 1 h post-injection (A) and 24 h post-injection (B), Published by Barrefelt et. al. in EJNMMI Research 2013, 3(1):12.

1.6   FLUORESCENCE IMAGING, IN VIVO IMAGING SYSTEM

Fluorescent dyes attached to MB or other vehicles are excited by light in a specific region, and are therefore suitable for imaging. Alexa-680 Vivo Tag (Perkin Elmer, USA) or fluorescein isothiocyanate (FITC) can be covalently attached to the polymer matrix of the MB, and the fluorescent MB can be studied under the microscope or in an IVIS system in animals. In combination with co-registration using CT, µCT and/or MRI, anatomical information can be obtained to show the exact organ location of uptake of the fluorescent marker. The IVIS® Spectrum, uses an optical imaging technology to facilitate non-invasive longitudinal monitoring of biodistribution and disease progression in living animals. An optimized set of high efficiency filters and spectral un-mixing algorithms makes it possible to take advantage of bioluminescent and fluorescent reporters across the blue to near infrared wavelength region. It also offers single-view 3D tomography for both fluorescent and bioluminescent markers that can be registered with our multimodality module to other tomographic technologies such as MRI, CT or SPECT/PET. For advanced fluorescence pre-clinical imaging, the IVIS Spectrum has the capability to use either trans-illumination (from the bottom) or epi-illumination (from the top) to illuminate *in vivo* fluorescent sources. 3D diffuse fluorescence tomography can be performed to determine source localization and concentration using the combination of structured light and trans-illumination fluorescent images. The instrument is equipped with 10 narrow band excitation filters (30 nm bandwidth) and 18 narrow band emission filters (20 nm bandwidth) that assist in significantly reducing auto fluorescence by the spectral scanning of filters and the use of spectral unmixing algorithms. In addition, the spectral unmixing tools allow the researcher to separate signals from multiple fluorescent reporters within the same animal. The basic principle of fluorescence is illustrated in a Jablonski diagram [53].

1.7   TARGETING

When studying a disease using an animal model, targeting is essential in directing the MB vehicle or nanoparticle to the site of disease. Streptavidin based microbubbles or nanoparticles can be used for tumor targeting with anti-Her2 Herceptin antibody, a biotinylated 1,4,7,10-tetraazacyclododecane-1,4,7,10-tetraacetic acid (DOTA) chelator labeled with ^{111}In for nuclear imaging as well as a biotinylated Cy5.5 fluorophore [54]. Anti-Her2 Herceptin antibody is widely used in the clinic in combination with chemotherapy for targeting and treatment of breast cancer [55].

Streptavidin can be attached to MB for further coupling of radioactive markers, fluorescence dyes, chelators or antibodies against inflammatory markers such as Vascular Cell Adhesion Molecule (V-CAM) and Intercellular Adhesion Molecule (ICAM), which could target inflammation [56, 57]. SPION MB have been targeted by Streptavidin, and work is performed to enable drug delivery to inflammatory tissue such as inflamed muscle.

1.8   THERANOSTICS AND DRUG DELIVERY

Despite extensive research during the past decades, cancer is still the second largest cause of death in developed countries. Cytostatic drugs are the corner stone of cancer treatment; however, these drugs are non-selective and have several side effects including CNS toxicity, growth disturbances in children, liver toxicity and kidney insufficiency. In the present work we investigated a new theranostic delivery system for chemotherapy by incorporating cytostatics into MB and microcapsules (MC). The use of polymer vehicles for theranostic devices is a promising future application of ligand functionalized SPION MB [58, 59]. This approach combines the imaging properties of MB by using SPECT/MRI with the MB:s ability to bind ligands and target disease by incorporating substances into their polymer matrix; such as doxorubicin, busulfan or dexamethasone. This enables the use of MB for theranostic purposes [60-70].

1.9   TRANSMISSION ELECTRON MICROSCOPY

Transmission electron microscopy (TEM) is an excellent tool for imaging and measuring the size of nanoparticles [20, 21]. Instead of light it utilizes electrons passing through an ultrathin specimen. An image is obtained from the interaction of electrons passing through the specimen. These electrons have a lower wavelength, which allows a resolution so high that even a single column of atoms can be detected. A "light source" at the top of the microscope emits the electrons that travel through vacuum in the column of the microscope. Instead of glass lenses focusing the light in the light microscope, the TEM uses electromagnetic lenses to focus the electrons into a very thin beam. The electron beam then travels through the specimen. Depending on the density of the material present, some of the electrons are scattered and disappear from the beam. At the bottom of the microscope the unscattered electrons hit a fluorescent screen, which gives rise to a "shadow image" of the specimen with its different parts displayed in varied darkness according to their density. The image can be studied directly by the operator or photographed with a camera. Microbubbles, nanoparticles and SPION patterns can be visualized using TEM. Micro- and nano vessel size can then be calculated [20, 21].

1.10 PERLS' PRUSSIAN BLUE STAINING AND IMMUNOHISTOCHEMISTRY

Perls' Prussian blue staining is commonly used to verify the presence of iron content in tissue and it can even distinguish single granules of iron in cells. By using haematoxylin and eosin (H&E) staining one can detect iron as brown pigments in tissue sections. However other pigments can show a similar color why haemosiderin should be differentiated from other brown pigments using the Perls' Prussian blue histochemical staining technique [20, 71, 72]. Moreover to show and visualize that SPION MB can be taken up by macrophages, CD68+ macrophages can be detected immunohistochemically [20]. This is shown in Figure 6.
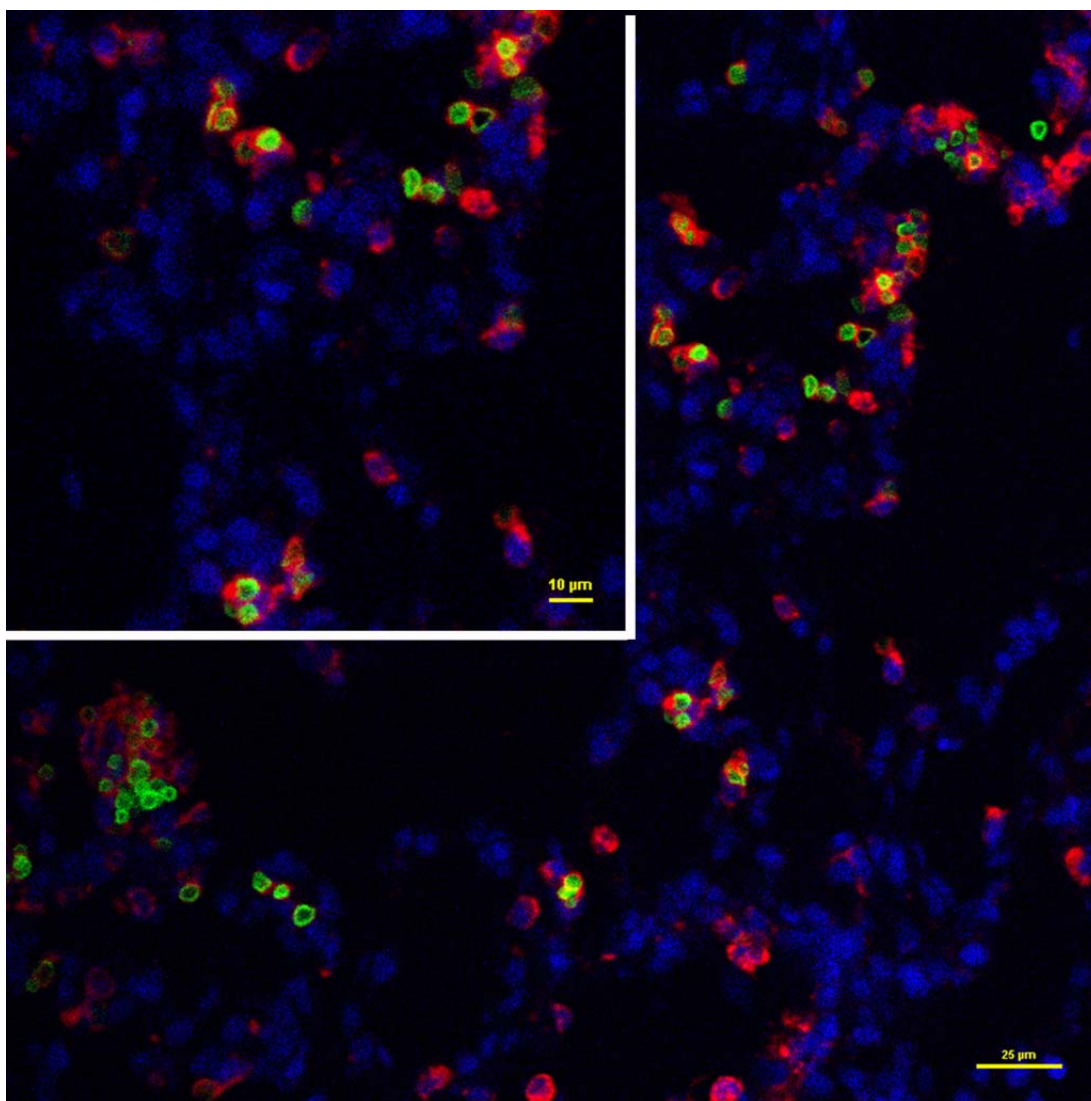
Figure 6. Intracellular localization of fluorescent SPION microbubbles inside labeled macrophages. A primary antibody against CD68 (red) confirms phagocytosis of the microbubbles (green) by macrophages in the lungs. The nuclei were stained blue using DAPI. The size bar represents 25 μm. The upper left part of the image is higher magnification with the size bar of 10 μm, Barrefelt et al. International Journal of Nanomedicine 2013:8(1) pages 3241 – 3254.

1.11 CONTRAST AGENTS

1.11.1 Microbubbles

In the current thesis, 3 μm single- and multiple layer PVA MB were used as a new contrast agent for multimodal imaging and theranostic applications. The thesis was carried out as part of the EU FP7 project 3MiCRON. Historically, MB were developed and used for ultrasound imaging due to their echogenicity after application of US waves [73-75]. Since the polymer matrix in MB is capable of functionalizing ligands for further binding of nuclear medicine markers and fluorescent markers, trapping and binding SPION and nanoparticles in their shell, MB can be used as an imaging vehicle for SPECT and MRI [17, 18, 20]. Tailoring the MB further by their size and lipophilicity might change their biodistribution, enabling imaging and drug delivery to several or different organs.

1.11.2 **SPION**

Several studies have shown that SPION can be easily tailored with targeting moieties, fluorescent dyes or therapeutic drugs [76]. SPION can also be used as potential anti-cancer agents for tumor therapy due to their cytotoxicity and/or their ability as drug carriers [77-79]. SPION with a size between 10 and 100 nm has a long enough circulation time to extravasate into the extra cellular space of tumors [80] and can be used in cancer imaging [81]. Polymer coated SPION have been reported to be useful as carriers for pharmaceutical drugs in slow release preparations and for magnetic hyperthermia [82, 83]. Iron particles from degrading SPION are eliminated in the body either through uptake by reticuloendothelial system (RES) cells (particles larger than 20 nm) or via renal filtration (particles with a hydrodynamic size of less than 5.5 nm) [81].

2 AIMS OF THE THESIS

2.1 GENERAL AIM

The aim of this thesis is to study the biodistribution and kinetics of microbubbles (MB) as a contrast- and theranostic agent using multimodal imaging.

2.2 SPECIFIC AIMS

1. To study the physical properties of MB as a MR contrast agent.

2. To study the pharmacokinetics and fate of single layer SPION MB as a contrast agent using MR imaging.

3. To study the biodistribution of ligand functionalized-, ^{99m}Tc labeled-, single- or multiple layer MB or SPION MB as a contrast agent in the rat using multimodal fusion imaging, SPECT/CT and SPECT/MRI.

4. To study the biodistribution, kinetics and biological fate of multiple layer SPION MB in rat organs.

5. To study the biodistribution of fluorescent Alexa-680 MB using multimodal fusion imaging, *in vivo* imaging system (IVIS)/μCT.

3 MATERIALS AND METHODS

3.1 MICROBUBBLE SYNTHESIS (STUDY I-V)

3.1.1 The Formation of Microbubbles (Study I, II, III, IV, V)

PVA shelled MB synthesis has been described elsewhere [84]. The synthesis can be summarized as follows: Poly (vinyl) alcohol (2 g); PVA 70K; (P1763, Sigma-Aldrich) was added to 100 mL of Milli-Q water. The suspension was stirred at 80°C to allow PVA dissolution. Sodium metaperiodate (0.19 g) was added to the solution and the mixture was stirred (1 h, 80°C). The solution was cooled to room temperature, with continuous stirring. The cross-linking reaction was carried out under vigorous stirring at room temperature (2 h, 8000 rpm) by an Ultra-Turrax T-25 equipped with a Teflon-coated tip. Floating MB were separated from solid debris and washed with Milli-Q water.

3.1.2 Formation of Single Layer Poly(Vinyl) Alcohol Microbubbles with Embedded SPION in the Shell (SPION MB) (Study I, II)

The synthesis of the PVA SPION MB has been reported previously [85]. Briefly, iron (II, III) oxide (Fe_3O_4) nanoparticles (SPION) with an average size of 8-10 nm were manufactured by mixing two acidic iron containing solutions, $FeCl_3 \cdot 6H_2O$ and $FeCl_2 \cdot 4H_2O$. The SPION were co-precipitated under vigorous stirring and addition of NaOH and thereafter collected using a magnetic bar and re-suspended in Milli-Q water. PVA was oxidized in Milli-Q water using sodium metaperiodate (1 h at 80°C) [84]. The PVA microbubbles containing SPION (20 mg/ml) were formed by adding the re-suspended SPION to the solution containing the oxidized PVA under stirring using Ultra Turrax (IKA-2000, Staufen, Germany), (8000 rpm, 2 h) to obtain SPION MB.

3.1.3 Chitosan Oxidation and Coupling to the Surface of Single Layer MB (Study III)

The metaperiodate ion, IO_4^-, cleaved the C2-C3 bond of the glucosamine residue of chitosan, which led to the formation of a di-aldehyde with the elimination of an ammonia molecule. However, the N-acetylated amino groups at the C2-position of the chitosan backbone (15 %) prevented the oxidation cleavage by metaperiodate. For the oxidation reaction, chitosan was dissolved in 1 % (w/v) distilled and de-mineralized water/HCl (pH = 4.5) and was thereafter mixed with a given amount of $NaIO_4$ (dark condition). A 2-fold molar excess of chitosan in relation to $NaIO_4$ was used. After 24 h the solution was dialyzed (dialysis membrane, MWCO of 2,000) against deionized water (pH = 4.5), lyophilized and stored as a freeze-dried powder. The oxidation that leads to chain de-polymerization as a side reaction increased the low solubility of chitosan in water and prevented cluster formation of the MB. The freeze-dried periodate oxidized chitosan was dissolved in D_2O (5% w/w TMS) at a concentration of 5 mg/mL. The resulting solution was subjected to ^{1}H-NMR examination and the degree of oxidation was calculated considering the integral of the C2-resonance at 3.00 ppm,

taking as reference the signal of the tri-methyl group of TMS at 0.0 ppm (9 H, TMS tri-methyl group). The oxidized chitosan was conjugated to MB by an acetalization procedure. The polymer was dissolved in Milli-Q water to a concentration of 1% (w/v). A sample of 20 mg aqueous MB suspension was added and the final volume was adjusted to 10 mL. The pH was carefully adjusted to 3.0 with 0.1 M HCl. The resulting suspension was stirred in the dark for five days at room temperature followed by extensive washing in separatory funnels and stored in Milli-Q water at 4°C.

3.1.4 Aminoguanidine Coupling (Study III, IV, V)

The MB suspension was centrifuged (30 g, 1 h) followed by removal of the subnatant. Aminoguanidine (5mg/mL) in HEPES buffer (0.1 M, pH = 8) was added and the suspension was kept on the shaker for 1 day. Afterward, the MB were washed three times. After each wash, the MB in the upper phase were separated by centrifugation (30 g, 1 h) and the subnatant was removed. Plain MB with a positively charged surface (amino groups) were obtained. The charged surface was necessary to further functionalize the MB by the different ligands: DTPA, PMAA, NOTA, NOTA-SPION and DTPA-SPION (Figure 1-I). MB were visualized using confocal laser microscopy at a resolution of 550 x 550 μm (Figure 1-II) (Leica TCS SPE, Leica Microsystems GmbH, Wetzlar, Germany). Size distribution was determined using flow cytometry (Partec CyFlow, ML, USA). Analysis of size distribution was performed using forward scattering versus side scattering. Figure 1-III shows DTPA-SPION MB.

3.1.5 Grounding by the Layer by Layer (LbL) Method [86] (Study III, IV, V)

Following the aminoguanidine (AG) grounding, the MB were coated using the layer by layer (LbL) technique and functionalized by different layers of poly(styrene)sulfonate (PSS) 70,000 / poly(ethylene) imine (PEI) 25,000 / PSS 70,000 / PEI 25,000 / PSS 70,000. The coating solutions consisted of 2 g/L in 50 mM acetate buffer (pH = 5.6) and 0.2 M NaCl. After each layer was added, the MB were washed four times followed by centrifugation to separate the upper phase (30 g, 40 min). The subnatant was then removed. This was followed by addition of the next layer obtaining a layer by layer LbL MB [86].

3.1.6 Preparation of DTPA MB (Study III)

The DTPA-isothiocyanate (0.2 mg DTPA/10^8 MB) was added to a suspension of AGMB (10 mM NaHCO$_3$, pH = 8). The reaction mixture was shaken overnight, washed and separated by centrifugation (30 g, 40 min). Polyamines in the top layer of the MB surface reacted with isothiocyanate (pH = 8) to form a stable isothiourea bond in molecules containing DTPA, which were functionalized onto MB.

3.1.7 **Preparation of Multiple Layer NOTA MB (Study III)**

NOTA-isothiocyanate (0.2 mg NOTA/10^8 MB) was added to a suspension of AGMB (10 mM NaHCO$_3$, pH = 8). The reaction mixture was shaken overnight and washed using centrifugation.

3.1.8 **Preparation of Multiple Layer PMAA MB (study III)**

The AGMB were coated in a standard PMAA (MW approximately 1×10^5 g/mol solution (pH = 6.2) for 1 day. The reaction mixture was washed using centrifugation.

3.1.9 **Synthesis of Multiple Layer Microbubbles Containing Fluorescein Isothiocyanate and Coating with Super Paramagnetic Iron Oxide (Study III, IV)**

The multiple layer SPION MB used in this PhD thesis were synthesized and produced as described previously [18]. Poly(vinyl) alcohol (PVA) was dissolved in water (20 g/L). 7.6 g of sodium periodate was then added and the mixture was incubated (85°C, 1 h), cooled to room temperature and suspended for 3 h using an Ultra Turrax (8000 rpm, IKA-2000, Staufen, Germany) followed by washing three times in a cream centrifugal separator (RZ OPS, 3000 rpm, Merryfarm, Kiev, Ukraine). The MB were modified with amino guanidine (AG) to enable further coupling with different layers according to the following procedure: the MB (100 mL, 7.1×10^{10} MB) were washed in 0.1 M HEPES buffer (pH = 8, 200 mL), aminoguanidine (5 mg/mL) was added and the suspension was put on a shaker for three days followed by washing and centrifugation. A poly(allyl) amine hydrochloride (PAH 15,000) layer was then attached to the MB to undercoat the magnetite. The coating solution contained 1 g PAH/L in a 50 mM acetate buffer (pH = 5.6) plus 0.1 M NaCl. The aqueous magnetite coating solution was added to the MB (12 mL/10^9 MB) plus 1 M acetate buffer (pH = 5.6) to obtain a concentration of 50 mM. NaCl (1 M) was added drop wise until the NaCl concentration reached 0.1 M. The sample was put on a shaker at room temperature overnight followed by the separation of the upper phase using centrifugation (30×g, 40 min). The subnatant was removed. From when the first magnetic layer had been attached to the MB, the solution was washed and separated in a magnetic field using a Neodymium magnet. This separation procedure was repeated for each layer. The MB (with the layers (Magnetic layer1)/PAH1/Magnetic layer 2/PAH2/Magnetic layer 3/PAH3) were coated by (2 x 80 mL PSS) per 5 x 10^{10} MB as described above. The negatively charged MB were washed and coated by 100 mL fluorescein isothiocyanate (FITC)-labeled PAH 15,000 (PAH-Flu) (1 g/L polyelectrolyte, 50 mM acetate buffer (pH = 5.6) and 200 mM NaCl, followed by an additional 100 mL PSS for coating and washing. A poly (allyl) amine hydrochloride (PAH) layer was attached to the MB to undercoat the iron oxide. PAH contains amine NH$_2$ groups that can react with Fluorescein isothiocyanate (FITC) to be labeled (pH = 8) overnight. The product was purified using dialysis. The negatively charged MB with PSS as outmost layer were then coated by the fluorescein labeled, positively charged PAH. Thereafter, the MB were again coated with PSS to provide a negatively charged surface.
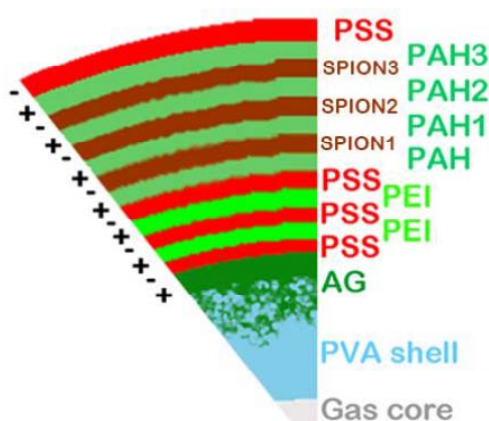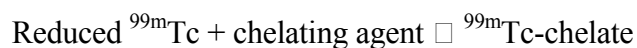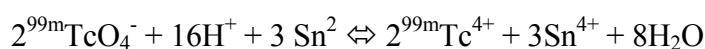
Figure 7. Showing the shell of a multiple layer MB consisting of a gas core, PVA shell, aminoguanidine (AG), Poly(styrene)sulfonate (PSS), Poly(ethylene) imine (PEI), Polyallylamine (PAH) with SPION between the PAH layers. By G. Egri, Surflay Nanotec GmbH, Germany.

3.1.10 Preparation of Multiple Layer Magnetic Microbubbles with NOTA (NOTA-SPION MB) or DTPA (DTPA-SPION MB) (Study III)

The AGMB were coated by layers of poly(styrene) sulfonate (PSS), poly(ethylene) imine (PEI) and poly (allyl) amine (PAH) as PSS 70,000/PEI 25,000/PSS /PEI/PSS/PAH. To this base, magnetite/PAH/magnetite/PAH/magnetite/PAH was attached using the Layer by Layer (LbL) technique [86]. When the first magnetic layer had been attached to the MB, they were washed and separated in a magnetic field. This procedure was repeated for each layer. The NOTA or the DTPA ligand was then coupled covalently to the outmost PAH-layer as described in section 3.1.5 and 3.1.6. The incorporation of SPION in MB was determined to 3.8 mg Fe/10^9 MB/mL.

3.1.11 ^{99m}Tc-MB Synthesis (Study III)

Reduced ^{99m}Tc is chemically reactive and can react with a chelating agent to become a ^{99m}Tc-chelate. The chemical group –COO$^-$ is the electron donor of DTPA and NOTA and NH$_2$ is the electron donor of chitosan as follows:

$$2\,^{99m}TcO_4^- + 16H^+ + 3\,Sn^2 \Leftrightarrow 2\,^{99m}Tc^{4+} + 3Sn^{4+} + 8H_2O$$

$$\text{Reduced }^{99m}Tc + \text{chelating agent} \quad ^{99m}Tc\text{-chelate}$$

Sodium pertechnetate (^{99m}Tc-NaTcO$_4$) was obtained from a ^{99}Mo/^{99m}Tc-generator. ^{99m}Tc was obtained using the reducing agent stannous chloride SnCl$_2$·2H$_2$O (Sigma-Aldrich, Germany). Plain-, chitosan-, DTPA-, NOTA-, PMAA-, DTPA-SPION- or NOTA-SPION MB (0.2 mL of 10^8 MB/mL) were diluted with 0.3 mL isotonic saline in 2 mL Eppendorf tubes. A half mL SnCl$_2$·2H$_2$O was added to the MB solution at room temperature. ^{99m}Tc-NaTcO^4 (0.5 mL) with an activity of 1000-1500 MBq (Dose Calibrator CRC®-15 PET, CAPINTEC INC. Pittsburgh, USA) was added to the ligand functionalized MB-SnCl$_2$ solution for the reduction reaction (5 min, pH = 5). The Eppendorf tubes were centrifuged (500 rpm, 4 min, Hettich Universal 16, Germany)

and the subnatants were removed. After centrifugation, isotonic saline was added and the procedure was repeated until the radioactivity in the subnatant was equal to or less than 5 % of the activity of MB in the upper phase of MB. To evaluate the stability of labeled MB, 0.2 mL (10^9 MB/mL) of DTPA functionalized MB and plain MB were labeled as above using 60 MBq. The MB were washed until less than 5 % remained in the subnatant. MB were resuspended in saline and followed during four half-lives of ^{99m}Tc.

3.1.12 Synthesis of Multiple Layer Alexa-680 Microbubbles (Study V)

The Alexa-680 MB were produced as described previously [18, 84, 86]. Poly (vinyl) alcohol (PVA) was added to de-ionized water and dissolved followed by Ultra Turrax T-25 mixing (8000 rpm, IKA-2000, Staufen, Germany) for 2 h. The aminoguanidine-MB (12 x 10^9 MB) aqueous solution was washed by centrifugation (60 g, 30 min) and the supernatant was removed. In order to enable optical imaging, the MB were fluorescence labeled by adding negatively charged Alexa-680 Vivo Tag (5 mg, Perkin-Elmer, USA) poly (allyl) amine hydrochloride (PAH) onto amino guanidine. $NaHCO_3$ (5 mL 50 mM) was added. The solution was stirred overnight and washed 3 times in the centrifuge followed by the addition of negatively charged poly(styrene) sulfonate (PSS) coating under standard coating conditions (2 g/L polymer in 50 mM acetate buffer and 0.2 M NaCl, 3 mL/10^9 MB). This was followed by washing using centrifugation.

3.2 ANIMAL STUDIES (STUDY I, II, III, IV, V)

The studies were carried out at Karolinska Institutet, approved by the Stockholm Southern Ethical Committee on Animal Research and performed in accordance with Swedish Animal Welfare law.

Male Sprague Dawley rats (study I-IV) weighing 300 g ± 50 g were purchased from Charles River (Charles River Laboratories, Germany). The animals had access to food and water *ad libitum* and 12 h light/dark cycle with controlled humidity (55% ± 5%) and temperature (21^oC ± 2^oC). The rats were anaesthetized using an intra-peritoneal injection of pentobarbital (sodium pentobarbital; 60 mg/mL, APL Kungens Kurva, Sweden) at a dose of 50 mg/kg. MR- and SPECT/CT imaging was performed on anesthetized, free breathing rats. The mice in study V were anesthetized using Isoflurane (Baxter Medical AB, Kista, Sweden) and placed prone, head first inside the IVIS system (PerkinElmer, Waltham, MA, USA).

3.2.1 Magnetic Resonance Imaging (Study I, II, III, IV)

The rats used for MR imaging were placed prone and "head in" in an extremity coil in the MR scanner (Siemens Trio, Siemens Medical Solutions, Erlangen, Germany) for imaging. They were imaged before and after an *intravenous* injection of ligand functionalized-, ^{99m}Tc labeled-, SPION MB or free SPION via the tail vein.

3.2.2 Nuclear Medicine (Study III)

The rats examined using nuclear medicine imaging were injected with functionalized DTPA-, PMAA-, chitosan-, NOTA-, NOTA-SPION-, or DTPA-SPION MB and placed prone in a vacuum pillow between the gamma camera heads (Siemens Symbia True Point 16 hybrid system, Symbia® Siemens, Erlangen, Germany), enabling dynamic scintigraphic measurements and tomographic SPECT/CT imaging.Rats injected with ^{99m}Tc labeled MB were sacrificed and their organs removed *post mortem* for radioactivity measurements using a Dose Calibrator (CRC®-15 PET, CAPINTEC INC. Pittsburgh, USA).

3.2.3 Histology (Study II, IV)

The rats that were examined histologically were injected with an intra-peritoneal (i.p.) injection of 60 mg/kg sodium pentobarbital and fixed onto a surgical pad in supine position. A surgical incision along the chest midline was made and the skin, the anterior part of the peritoneum and the diaphragm were cut. The right atrium was incised to release intravascular pressure and 40 mL of heparinized PBS and 60 mL of ice-cold fixation solution (paraformaldehyde (PFA), 4 %, Solveco, Sweden) were injected very slowly through a needle inserted in the left ventricle. The perfusion of the corporal circulation was monitored by observing the liver turning pale. Tissues were then dissected and transferred to 4 % PFA. After 48 h the PFA was replaced by 70 % ethanol before further dehydration and paraffinization of selected tissue samples in a vacuum infiltration processor. The organs were embedded in paraffin according to RENI trimming guidelines [87-89]. The blocks were sliced, mounted for examination under the microscope.

3.2.4 In Vivo Imaging System (Study V)

FVB/N mice were purchased from Charles River (Charles River Laboratories, Sulzfeld, Germany) and had free access to food and water, 12 h light/dark cycle, controlled humidity (55 % ± 5 %) and temperature (21°C ± 2°C). The mice were injected *intravenously* with MB into their lateral tail vein, while awake in a mouse strangler. Prior to image acquisition, the mice were anaesthetized using 2-3 % Isoflurane (Baxter Medical AB, Kista, Sweden). Isoflurane (1-2 %) was used for anesthesia maintenance. The anesthetized mice were placed dorsal side up in a Mouse Imaging Shuttle (MIS) and imaged using IVIS 2D, -3D tomography at 30 min, 2 h, 4 h and 24 h post-injection followed by Quantum FX-μCT (PerkinElmer, Waltham, MA, USA) and Visual Sonic ultrasound (Vevo 2100 (FUJIFILM VisualSonics Inc., Toronto, Canada).

3.3 MEDICAL IMAGING

3.3.1 Magnetic Resonance Imaging Protocol (Study I, II, III, IV)

The MR examinations in this thesis were performed using a commercially available 3 T MR system (Siemens Trio, Siemens Medical Solutions, Erlangen, Germany) [18, 85, 90]. An extremity coil was used for imaging. A home-made T2 star (T2*) sequence developed for measuring iron oxide content was used with 12 echo times (TE) and 1.9

ms increments. The contrast agent was injected *intravenously* into the tail vein of anaesthetized rats. Imaging was performed using a gradient echo T2* sequence to obtain images with a fixed repetition time of 2000 ms and 12 stepwise increasing echo times (TEs) of 2-22.9 ms. Field of view read was 250 mm with a phase encoding of 59.4 % and a slice thickness of 3 mm. Circular ROIs were placed manually in the respective organs on areas with a small standard deviation of <100 mm. The negative logarithmic values of the signal intensities at different TEs were plotted versus the respective TEs followed by the calculation of T2*. In organs with short T2*, the calculations of T2* were based on fewer measurement points, excluding those with long TEs where full transaxial relaxation had already occurred [18].

3.3.1.1 Study 1

Phantoms and animals were scanned using 3 T MRI pre- and post-injection of 0.5 mL of 4.7×10^8 single layer SPION MB/mL through the tail vein.

3.3.1.2 Study 2

MR Phantom Study:
The SPION MB solution was analyzed using inductively coupled plasma atomic emission spectroscopy (ICP-AES) (Thermo Scientific iCAP 6500, Thermo Fisher Scientific, Waltham, MA, USA) to determine the concentration of iron oxide (Fe_3O_4). Three phantoms containing SPION MB were produced by agarose (Sigma-Aldrich Sweden AB, Stockholm, Sweden), which was mixed into water to obtain a concentration of 3 w %, then heated to 85°C. The hot, liquid agarose gel was poured into Falcon tubes (Thermo Fisher Scientific Inc., Waltham, MA, USA) and mixed with SPION MB to obtain three concentrations of Fe_3O_4 (0.125, 0.25 and 0.5 mM) followed by cooling to RT. The SPION MB agarose phantoms were imaged at 3 T (Siemens Trio, Erlangen, Germany) using the extremity coil and a T2* sequence with 12 increasing echo times of 2 ms to 22.9 ms [85]. Regions of interest (ROIs) were drawn on the phantom MR images and the signal intensity was measured in each ROI. This was followed by the calculation of the spin-spin relaxation rate (R2*) for each phantom. R2* was plotted against its Fe_3O_4 concentration, to obtain a standard curve.

MR Animal Study:
The animals were injected with 0.75 mL of $1x10^9$/mL single layer SPION and scanned dynamically at 3 T MRI. The MR scans were repeated pre injection and post-injection until 2 h and then at 24 h, 48 h, 72 h, 1 w, 2 w, 3 w and 4 w.

3.3.1.3 Study 3

The rats were injected *intravenously* with 0.5 mL during dynamic scintigraphic measurement and imaged prone using fusion SPECT/CT. The animals injected with MB containing SPION were brought to the MR scanner for co-registration to enable fusion SPECT/MR imaging. Each of the animals injected with SPION MB was examined 1-2 times using MRI.

 Several (up to 10) MRI examinations at 3 T using T2* were performed at different occasions on each animal to enable pharmacokinetic calculations after the injection of fluorescent FITC-SPION MB (0.5 mL, 1×10^9 MB/mL) i.v into the tail vein of the rats. The animals were free breathing and anesthetized using an intra-peritoneal injection of Pentobarbital. The animals were taken back to their cages between MR scans and allowed to rest for at least 24 h before the next imaging session.

3.3.2 Nuclear Medicine Imaging: Dynamic planar Scintigraphy and Single-Photon Emission Computed Tomography / Computed Tomography Protocols (Study III)

SPECT/CT imaging was performed using a Siemens Symbia True Point 16 hybrid system (Symbia® Siemens, Erlangen, Germany) with parallel hole LEHR collimators [18]. The dynamic planar scintigraphy (2 frames per second) was carried out with a total duration of 11.4-11.7 minutes. The matrix size was 256 x 256 with a 15 % wide energy window for ^{99m}Tc and the SPECT matrix size was 128 x 128. SPECT was performed with 64 projections over 360°, non-circular, step and shoot mode. The duration of each projection was 60 seconds. The total acquisition time required for SPECT was 32 minutes. Immediately after the SPECT acquisition, a CT scan was performed with a tube current of 110 kV, quality ref mAs was 160 mAs modulated with CareDose4D®, rotation time of 0.6 seconds and pitch 1.0. The CT data was reconstructed with a slice thickness of 0.75 mm and a "B70s sharp" kernel. A 3D Gaussian post filter (0.8 cm FWHM) was finally applied. Regions of interest (ROIs) were outlined for the organs on the dynamic images and counts were measured in each ROI using the Hermes system. No correction for radioactivity decay was made due to the short time interval. The number of counts in each organ was compared to the total counts in the whole animal to obtain the percentage of distribution to each organ. Interpretation of fused SPECT/CT images was made in three orthogonal planes. Reconstruction of the SPECT data and evaluation of the resulting images as well as fusion of SPECT/CT and SPECT/MR images were made on a Hermes workstation (Hermes Medical Solutions AB, Stockholm, Sweden). For SPECT/MR fusion the MR images were imported from the Picture Archiving and Communication System (PACS) to the Hermes system and then overlaid with the respective SPECT image to obtain fusion SPECT/MRI, which shows both anatomy and function in the same image. Iterative reconstruction was made with ordered subset expectation maximization (OSEM 4 iterations, 8 subsets, including resolution recovery). A phantom was made using agarose with three parallel vessel sized holes transversal through the phantom. For imaging the respective holes were injected with ^{99m}Tc labeled chitosan MB.

3.3.3 Ultrasound Protocol (Study I, V)

In order to preliminarily evaluate the MB distribution in specific organs, ultrasound imaging was performed in mouse liver, kidney and spleen tissue before injection and in mouse liver, kidney and spleen tissue 24 h post-injection using a high frequency ultrasound system, Vevo 2100 (FUJIFILM VisualSonics Inc., Canada). Ultrasound images were obtained both in b-mode (liver imaging: f = 18 MHz, frame rate = 18/s; kidney and spleen imaging: f = 21 MHz, frame rate 10/s) and in non-linear contrast mode (f = 18 MHz, frame rate = 18/s). Prior to image acquisition, the mice were anesthetized utilizing 3-4 % Isoflurane (Baxter Medical AB, Kista, Sweden), and anesthesia was maintined using Isoflurane (1-2 %, Baxter Medical AB, Kista, Sweden). During anesthesia, the body temperature was controlled by a heating pad. In addition, heart rate and respiratory frequency were monitored.

3.3.4 *In Vivo* Imaging System Protocol (Study V)

Imaging was performed using IVIS spectrum 2D and Quantum FX (PerkinElmer, Waltham, MA, USA). Fluorescent images were taken using the following Excitation/Emission filter pairs: 640/680nm, 675/720nm, 675/740nm, 675/760nm and 675/780nm. The spectral un-mixed 2D image (fluorescence photograph) was acquired with epi-illumination as a reference to verify the location of uptake and to select trans-illumination locations. The mice were imaged using a 3D FLIT imaging sequence that was acquired at excitation 675 nm and emission 720 nm. After *in vivo* imaging of Alexa-680 MB distribution, the organs (lungs, liver, spleen, kidneys) were removed and imaged separately *post mortem* with 2D epi-illumination fluorescence imaging, using a filter pair of 675/720nm. 3D FLIT image reconstruction, spectral un-mixing for auto fluorescence background removal, FLIT-CT co-registration and fluorescence efficiency quantification were generated using Living Image® 4.2 software (PerkinElmer, Waltham, MA, USA).

IVIS imaging was performed using both 2D and 3D tomography *in vivo* as well as 2D *ex vivo* on the organs *post mortem*. The mice were anesthetized using Isoflurane (Baxter Medical AB, Kista, Sweden) and placed prone, head first inside the IVIS system. The option for imaging fluorescent nanoparticles using the epi-illumination mode was chosen, and was followed by spectral un-mixing. The excitation filters chosen ranged between 500-780 nm and the emission filters chosen ranged between 640-780 nm. Initially, a 2D image (fluorescent photograph) was acquired with epi-illumination to verify the location of uptake. Thereafter, the mice were imaged using the 3D mode surface tomography (FLIT) with trans-illumination. The CT images were co-registered to show the anatomical map of the mice.

3.3.5 Small Animal Computed Tomography (Study V)

The mice were scanned and co-registered using computed tomography (CT). The mouse was placed prone in the co-registration shuttle MIS, sequentially imaged and subjected to a CT scan with a field of view at 75 mm, with three minutes X-ray exposure (Varian Medical Systems, Salt Lake City, UT, USA).

3.4 PHARMACOKINETIC MODELING

After MR measurement of R2* in rat liver the baseline value was subtracted, and the corresponding iron oxide concentration for each R2* value was read from the standard curve. The concentration data in the rat liver was fitted to a one-compartment open model[18]. Parameters such as elimination rate constant, maximum concentration (C_{max}) and micro constants were estimated. The area of the concentrations *versus* time (AUC) was calculated from the model-derived parameters and the elimination half-life was calculated from the slope of the terminal phase of elimination. Pharmacokinetic modeling was performed using WinNonLin version 5.0 (Pharsight, Mountain View, CA, USA). The mean, median and standard deviation (SD) of all parameters were calculated using GraphPad (version 4.0, Graph Pad, San Diego, CA, USA). All values are presented as mean ± SD.

3.5 HISTOPATHOLOGY (STUDY II, IV, V)

3.5.1 Perls' Prussian Blue Staining and Quantification

For histological quantification of MB in tissues, Perls' Prussian blue stained slides were digitally scanned using a 3D HISTECH Panoramic slide scanner (3DHISTECH, Budapest, Hungary). Repeated measurements of a minimum area of 1 mm^2 was selected for lungs, liver and spleen (n = 5) from each animal for digital counting of MB based on their iron content, using Nikon Elements BR-software (Nikon Instruments Inc., Melville, NY, USA).

3.5.2 Immunohistochemistry

To confirm the phagocytosis of MB by macrophages in organ tissue from liver, spleen and lungs, immunohistochemistry was performed with a primary antibody against CD68 macrophage marker (MCA 341, AbD Serotec, Kidlington, Great Britain). The secondary antibody was alkaline phosphatase conjugated rabbit anti-mouse (Sigma A4312, Sigma, St. Louis, MO, USA). The Vector red substrate (Vector, SK5100, Vector Laboratories Inc., Burlingame, CA, USA) produced a red signal for bright field as well as red fluorescent microscopy. The slides were cover slipped utilizing DAPI containing mounting medium (Vector VECTASHIELD® H1200, Vector Laboratories Inc) to produce nuclear counter stain and the slides were further evaluated using a confocal microscope with appropriate fluorescence filters for FITC, Cy5 and DAPI (Nikon A1R, Tokyo, Japan).

3.6 THERANOSTICS AND DRUG DELIVERY

3.6.1 Busulfan Labeled Microbubbles

The cytostatic Busulfan (Bu) was dissolved in dimethyl sulfoxide (DMSO) (50 µl) and mixed with 50 µl 10^8 pre-formed MB/mL. The Bu-MB sample was incubated at room

temperature on a wheel rotator for 72 h. DMSO was taken up by MB, which were transformed into microcapsules (MCs). The MCs were dialyzed and the dialysate was replaced at 2, 4, 6 and 24 h. The microcapsules were harvested, washed, re-suspended in acetonitrile and analyzed using gas chromatography (GC) with an electron capture detector.

In another experiment, the microcapsule pellet containing Bu was resuspended in 200 µl isotonic saline. Tin chloride ($SnCl_2$) and sodium pertechnetate (69.7 MBq) were added to the MCs and reduction was allowed to take place for 5 minutes. The sample was washed with isotonic saline and centrifuged at 500 rpm for 4 minutes. Activity was measured to be 0.74 MBq in the supernatant and 10.8 MBq in MCs (93 % pure). 0.5 mL of ^{99m}Tc labeled busulfan MCs (2.5 MBq) was thereafter injected i.v. into the tail vein of a Sprague Dawley rat. Dynamic gamma camera measurement was carried out for 684 seconds followed by SPECT/CT (Siemens Symbia) using 64 projections, 60 seconds/angle.

3.6.2 ^{99m}Tc Labeled Dexamethasone-DOTA-SPION Microbubbles for the Treatment of Muscle Inflammation in Rat

The content of one Eppendorf tube of freeze-dried Dexamethasone-1,4,7,10-tetraazacyclododecane-1,4,7,10-tetraacetic acid (DOTA)-SPION MB (dexamethasone 21-acetate (DMA) from lyophilized MBspH5RT/b-cyclodextrins) was dissolved in 1 mL saline and labeled with ^{99m}Tc. A start activity of 291 MBq/mL of Tc-pertechnetate was added in addition to the MB. A Sprague Dawley (480 g) rat was sedated using Isoflurane and anesthetized using an intra-peritoneal (i.p.) injection of 0.35 mL Pentobarbital (60 mg/mL, APL, Kungens Kurva, Sweden). The hair was removed on both hind legs using hair removal cream (Veet). A wireless Bluetooth gamma probe (neoprobe® GDS Gamma detection system) was utilized to measure the local number of counts in the organs of the rat by placing the gamma probe vertically towards/on the skin over the target organ. A circular 7 mm Neodymium Iron Boron NiCuNi coated 2500 Gauss magnet (Panduro, Sweden) was attached with tape onto the skin of the right hind leg calf muscle followed by an *intravenous* (*i.v*) bolus injection of ^{99m}Tc labeled MB (60 MBq, 1 mL).

The magnet was removed and the rat was placed prone, head first, under the gamma camera (Siemens Symbia True Point 16 hybrid system (Symbia®, Siemens, Erlangen, Germany) and scanned using dynamic planar scintigraphy (2 s, 150 frames) for 300 s. The matrix size used was 256 × 256 and a suitable energy window for ^{99m}Tc was used, 15 % wide. Immediately after the dynamic imaging, a SPECT tomography was run using a 128 × 128 matrix, 64 projections over 360° of 60 sec/projection, non-circular orbit, step-and-shoot mode. The acquisition time required for SPECT was 32 min. The CT scan was performed with a tube current of 110 kV, quality reference was 160 milliampere sec (mAs), modulated with CareDose4DW; rotation time was 0.6 sec, and the pitch was 1.0. Subsequently, the CT data was reconstructed with a slice thickness of 0.75 mm and a "B70s sharp" kernel. Reconstruction of the SPECT/CT images was

done on a Hermes workstation (Hermes Medical Solutions AB, Stockholm, Sweden). The iterative reconstruction was done with ordered subset expectation maximization (four iterations, eight subsets, including resolution recovery). A 3D Gaussian post filter (0.8 cm FWHM) was finally applied. After 14 h the rat was re-scanned using dynamic imaging and SPECT/CT.

The rat was scanned pre- and post-injection (2 h post-injection and 24 h post-injection) using a 3 T MR scanner (Siemens Trio, Siemens, Erlangen, Germany). The rat was placed head first, prone, in an extremity coil. Imaging was performed using a gradient echo T2*sequence to obtain images with a fixed repetition time of 2000 ms and 12 stepwise increasing echo times (TEs) of 2 to 22.9 ms. Field of view was 250 mm with a phase encoding of 59.4 % and a slice thickness of 3 mm. Circular ROIs were placed in the respective organs, and the negative logarithmic values of signal intensities at different TEs were plotted versus respective TE values followed by calculation of T2*. Coronal and transversal T2 Turbo Inversion Recovery Magnitude (TIRM) sequences were run with fixed TE of 80 ms, fixed TR of 5000 ms and flip angle 120. The sequence is sensitive to denervated or inflamed muscle preceding muscle atrophy. T2 HASTE coronal was applied with TE = 91 ms, TR = 2000 ms and flip angle = 150.

4 RESULTS

4.1 MICROBUBBLE SYNTHESIS

Plain MB, single layer SPION-, chitosan MB, multiple layer DTPA-, NOTA-, PMAA-, SPION-, DTPA-SPION-, NOTA-SPION-, 99mTc-labeled FITC-SPION-, Alexa-680 MB as contrast media for imaging were manufactured as described above. The MB were not shown to aggregate in water solution, nor did they contain any debris seen by visual inspection in the light microscope (Figure 8A and B). Figure 8A shows the SPION MB labeled by fluorescent FITC. High resolution TEM reveals that the SPION MB particles have an average diameter of ca. 3.1 µm (Figure 8C). The single crystal structure of SPION, embedded in between the shell layers of SPION MB, were measured to have an average size of 12.4 nm (Figure 6D). Moreover using forward scattering (FSC) flow cytometry shows the size distribution to be around 80 as a mean showing that SPION MB were not aggregated nor contained debris; while using sideward scattering (SSC) gave us information about the surface.
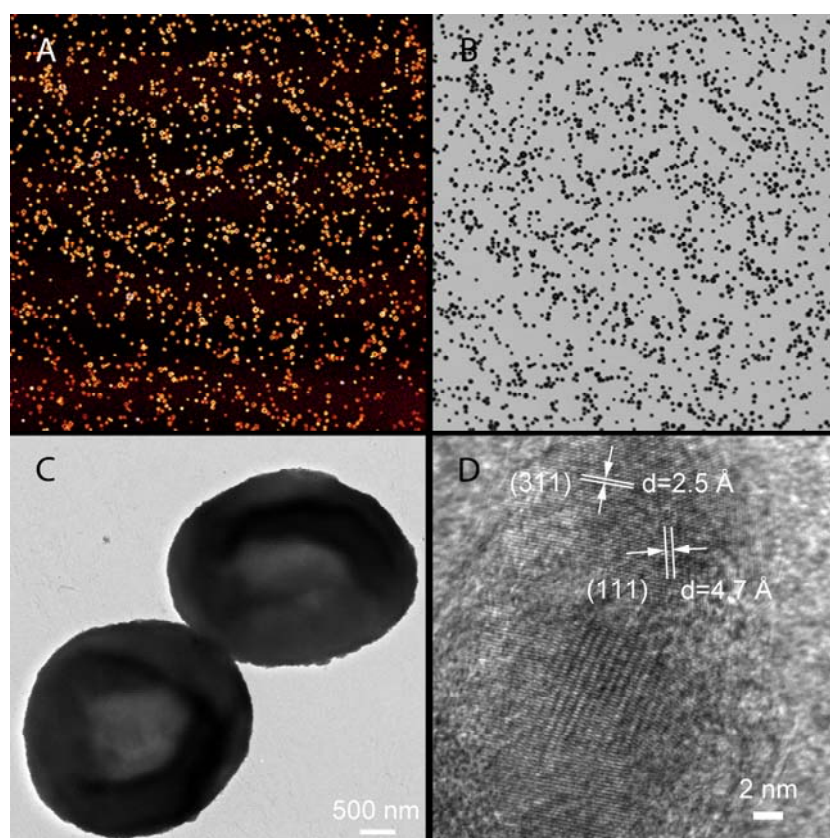
Figure 8. SPION MB visualized in the light microscope (image size 550 µm x 550 µm, Leica TCS SPE) using the FITC channel (A) and in bright-field microscopy setting (B). Two microbubbles (MBs) seen in the electron microscope (C) and crystal lattice parameters of SPION (D) using JEOL JEM-2100F field emission transmission electron microscopy (FE-TEM), Barrefelt et. al., International Journal of Nanomedicine 2013:8(1) pages 3241 – 3254.

4.2 MAGNETIC RESONANCE IMAGING

Agarose phantoms were mixed with SPION MB. Figure 7 shows two phantoms imaged at TE = 2 (A), 3.9 (B) and 5.8 ms (C). The phantom in the top row contains agarose gel while the phantom in the lower row contains SPION MB at a concentration of 0.5 mM. The MR signal intensity in the phantom containing SPION MB decreases with increasing TE (bottom row); while the signal in the phantom with only agarose gel stays rather constant. The signal decrease in the phantoms containing SPION MB enables the calculation of T2* and R2* for the calculation of a standard curve. The iron oxide (Fe_3O_4) concentration of the SPION MBs was calculated to be 4.73 mM (265 ppm) as measured using ICP-AES. The standard curve (R2* versus [Fe_3O_4]) was calculated from R2*.

Sprague Dawley rats were injected *i.v.* with either single- or multiple layer SPION MB, 2 h after which the T2* value of the liver had decreased to its minimum (Figure 8). After injection of SPION, the liver T2* reached its minimum in less than 1 h. The elimination half-life of SPION MB was 598.2 ± 97.3 h for single walled PVA MB, while for multiple walled SPION MB the half-life was 741 ± 219 h and for free SPION 222.6 ± 26.4 h. Using histopathology, by Perls' Prussian blue staining and immunohistochemistry we showed that single layer SPION MB, SPION and plain MB were accumulated in the liver through macrophage uptake and were then slowly eliminated.

Multiple layer fluorescent FITC-SPION MB were injected into rats to determine their biodistribution, biological fate and kinetics using MR imaging and histopathology. By staining CD68+, histopathology could show the uptake of the FITC-SPION MB by macrophage uptake in the liver and spleen. Histological findings were correlated with MR imaging since we could detect iron uptake by Perls' Prussian staining and for the same time points also detect signal decrease on T2* weighted images.

The rats injected with multiple layer, ligand functionalized, ^{99m}Tc-labeled DTPA SPION MB were co-registered using hybrid SPECT/CT and MR imaging. By fusion of the images we could detect uptake of DTPA-SPION MB primarily in the lungs at 1 h post-injection while the MB could be seen in the liver at 1 h and 24 h post-injection.
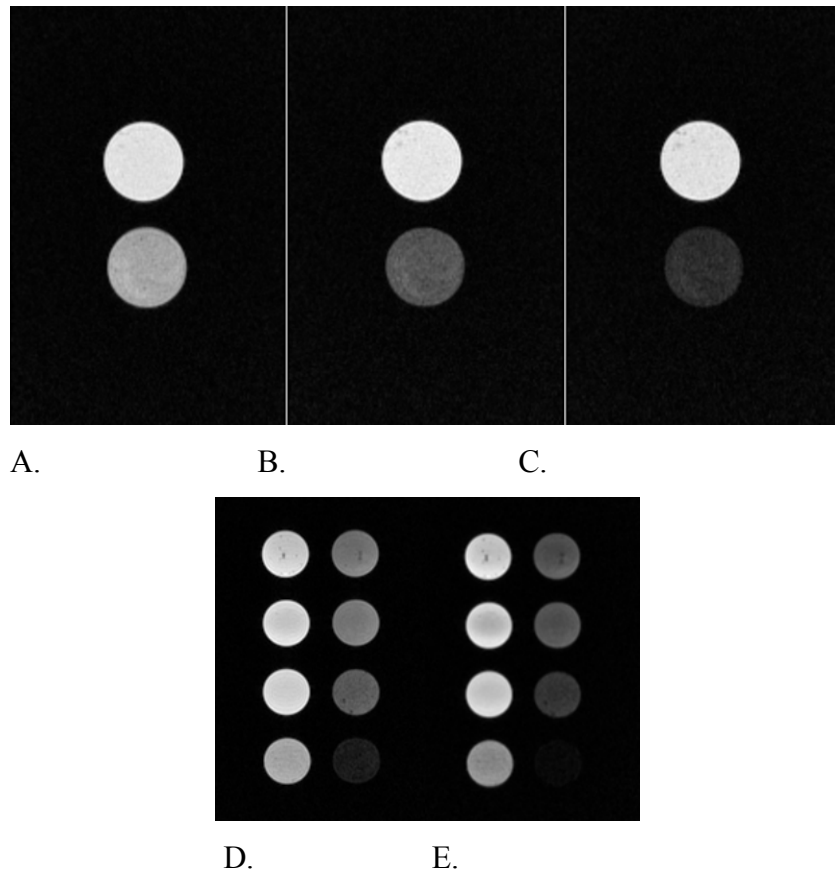
Figure 9. Agarose phantoms containing SPION MB imaged at 3 T MRI. The signal intensity is relatively constant in the agarose phantom without iron oxide (uppe row), but decreases with increasing echo time, TE = 2 (A), 3.9 (B) and 5.8 (C) ms, in a phantom containing SPION MB. Phantoms of increasing SPION concentration (C = 0, 0.01, 0.02, 0.03, 0.04, 0.05, 1 and 2 mM) were imaged at TE = 3.9 (D) and 5.8 (E) ms. This shows that by increasing TE values, the signal intensity and T2* decrease; hence this leads to an increase in R2*.
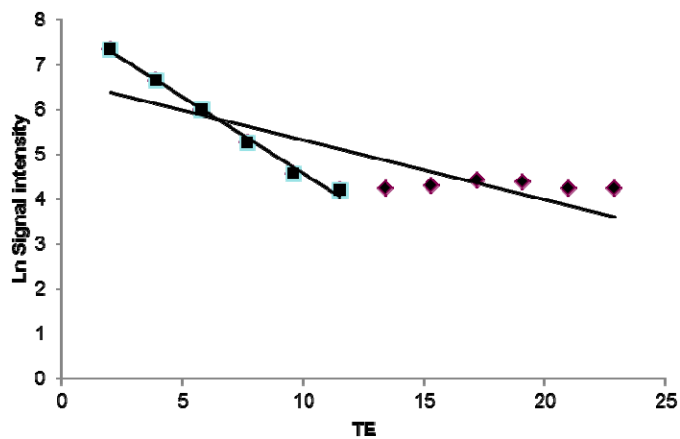
Figure 10. The negative logarithmic values of the signal intensities at different TEs are plotted versus the respective TE value (ms). The spin-spin relaxation time, T2 star (T2*), could then be calculated as the slope of the semi-log plot of the signal intensity versus the echo times (TEs). This image shows that due to fast decay only the first TE values (TE = 2-11.5 ms) can be used for calculating slope of the curve. If all TEs would be used for the calculation, this would lead to underestimation of the slope, as can be seen from the straight line going through TE = 2-22.9 ms.
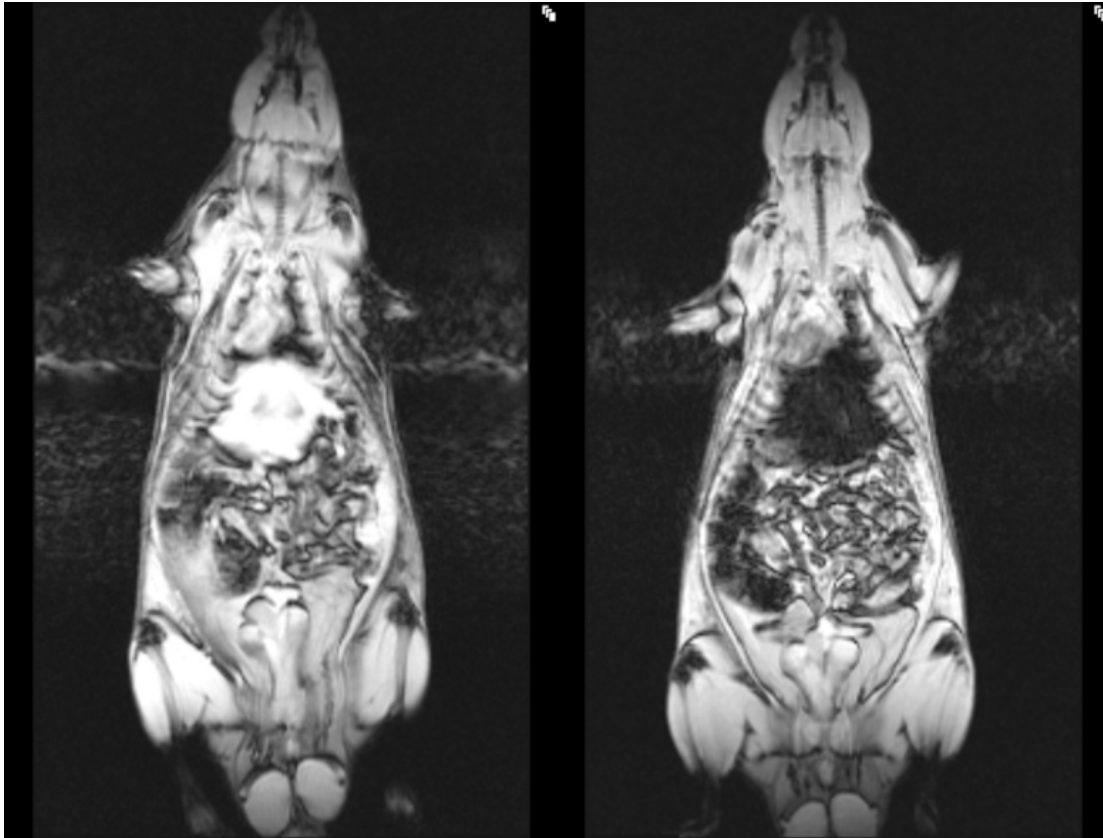
Figure 11. T2 weighted 3 T MR image (Siemens Trio, Siemens, Erlangen, Germany) showing one rat imaged using the T2* sequence. The left image shows the rat pre-injection, while the right image shows the rat post-injection. Signal decrease on the T2* weighted images can be visualized in the liver of the rat, which shows that SPION MB are uptaken primarily in the liver. This was confirmed by R2* calculations; which shows that R2* increase in the liver post-injection.
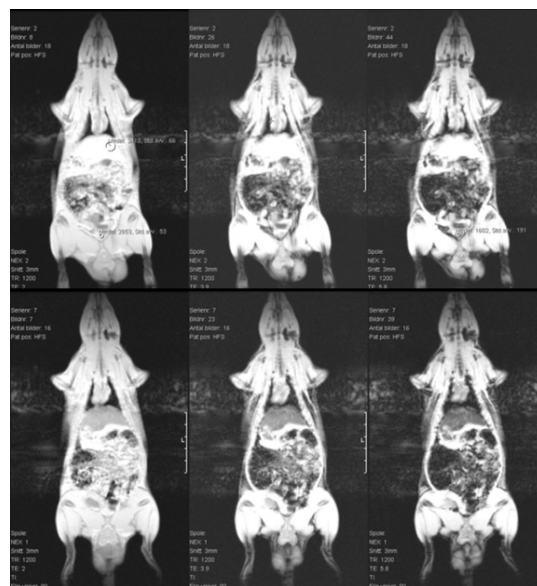
Figure 12. The 3 T MR image shows the same rat imaged using three echo times, TE = 2, TE = 3.9 and TE = 5.8 ms. The images in the upper row shows a non-injected rat; while the images in the lower row shows the same rat injected with SPION MB. One can see that as the TE value increases, the signal intensity in the liver tissue decrease (left to right).

4.3 NUCLEAR MEDICINE IMAGING

Fusion SPECT/CT and MRI showed that the biodistribution of ^{99m}Tc-labeled ligand functionalized MB varied with the type of ligand. One h post-injection of ^{99m}Tc-labeled DTPA- and chitosan MB, the highest uptake was observed in the lungs, while PMAA MB were evenly distributed between the lungs and the liver. The highest counts of ^{99m}Tc labeled NOTA-SPION and DTPA-SPION MB were observed in the lungs, liver and kidneys 1 h post-injection, while the highest counts were observed in the liver, spleen and kidneys at 24 h post-injection as confirmed by MRI. MR shows a signal decrease in the liver but, due to the uptake of ^{99m}Tc labeled MB in the liver, there is overlap and the signal decrease cannot be detected. However, the MR image provides an anatomical map of the rat. Fusion SPECT/CT enables us to see the anatomical structures of the rat.
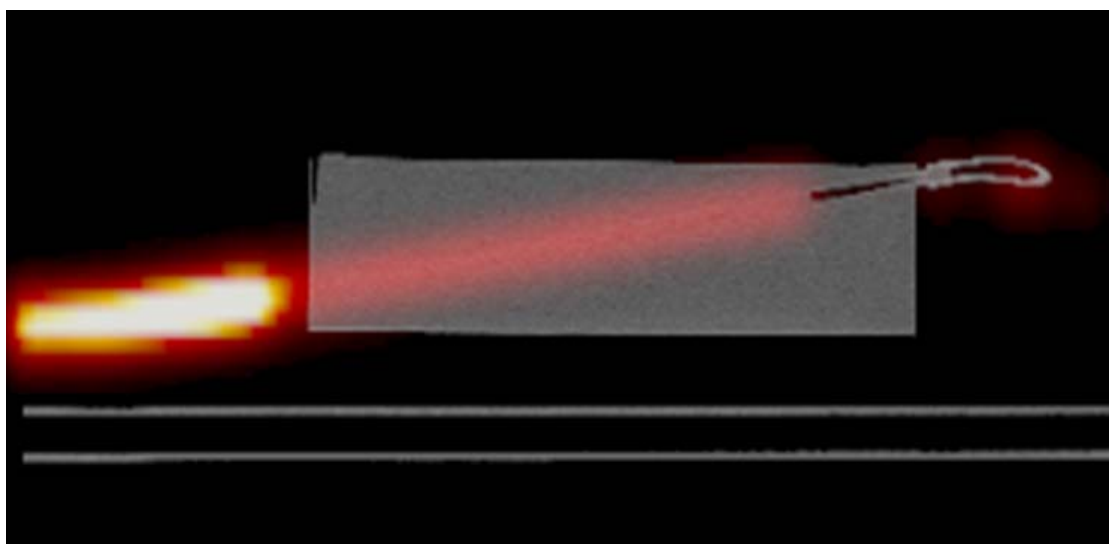
A.
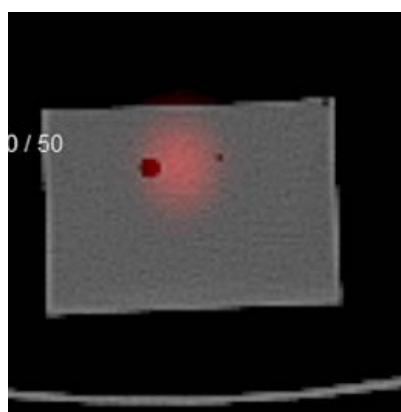
B.

Figure 13. An agarose phantom imaged using SPECT/CT. (A) is sagittal view, while (B) shows the phantom in the coronal view. ^{99m}Tc labeled MB were injected into the middle, rat sized aorta. The middle aorta is isodense on the CT image (B). The SPECT image (B) is more blurred, which shows that the resolution is less in SPECT than in CT.
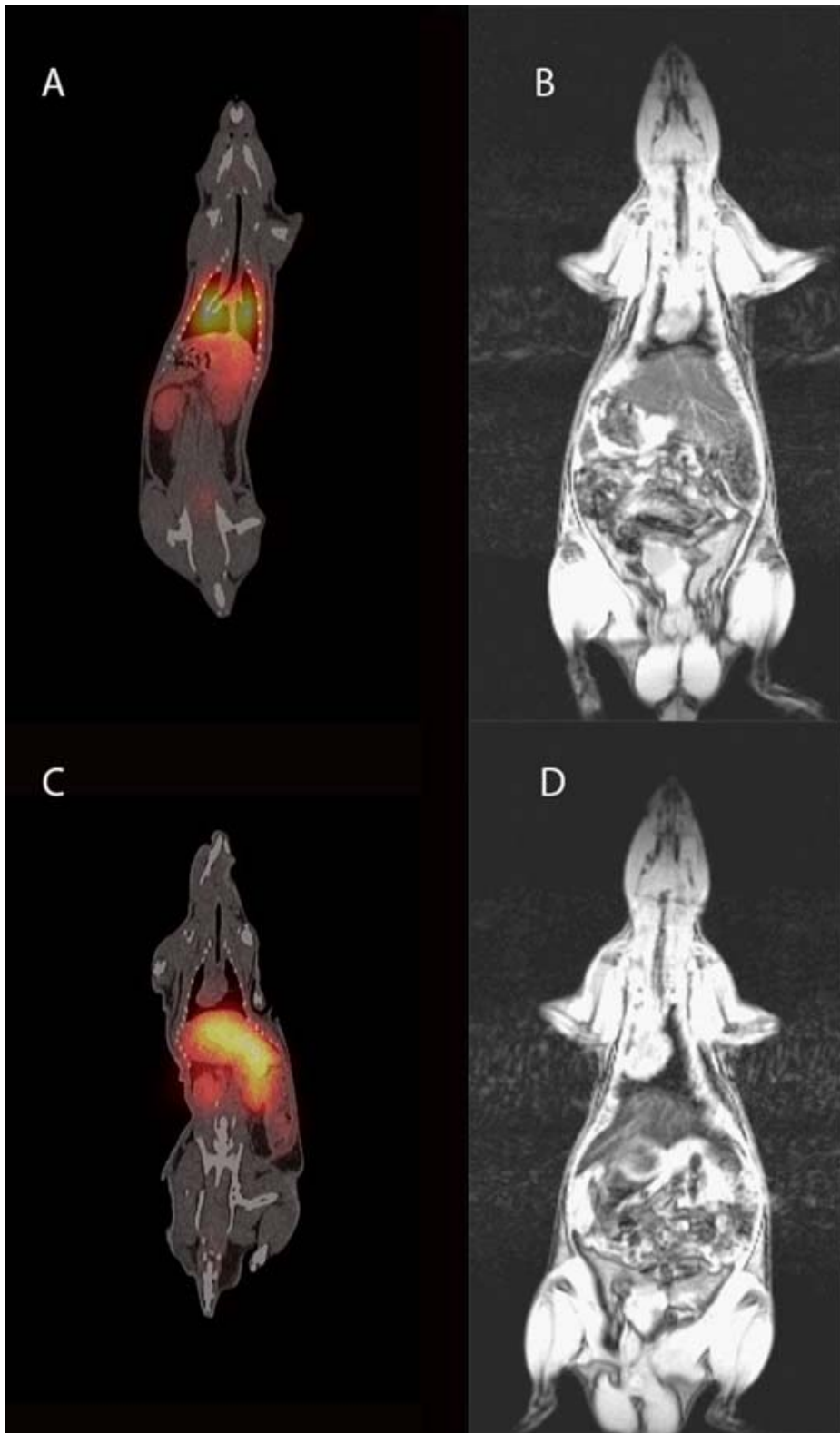
Figure 14. A rat imaged prone using SPECT/CT (A) and 3 T MR (B) 1 h post-injection of NOTA-SPION MB. The image shows primary uptake of MB in the lungs and liver on the SPECT image while the MR image cannot show uptake in the lungs due to air, but signal decrease is detected in the liver (B). After 24 h the MB have redistributed to the liver and spleen (C). The findings from imaging were confirmed by measuring radioactivity in organs *post mortem*. At 24 h post-injection using 3 T MRI we can detect signal decrease (MB) in the liver with decreased intensity compared to 1 h post-injection. Published by Barrefelt et. al. in EJNMMI Research 2013, 3(1):12.

.
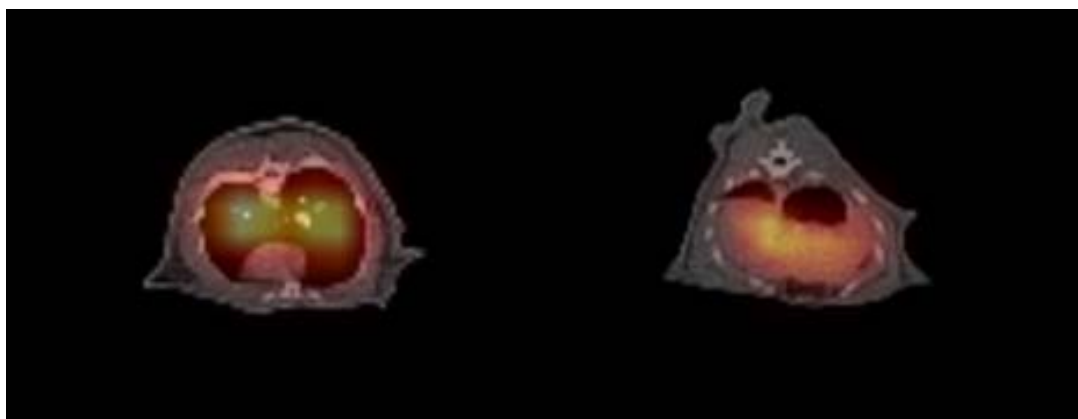
A.   B.

Figure 15. The rat from Figure 14 is imaged using SPECT/CT in the transversal plane. At (A), 1 h post-injection, MB are found in the lungs, while at (B), 24 h post-injection, MB are visualized in the liver.
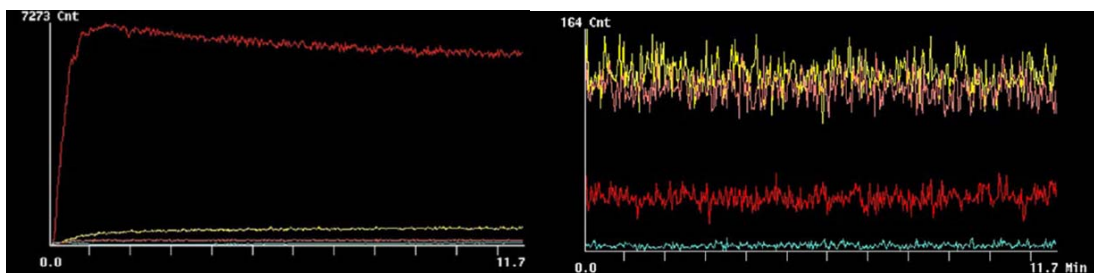
Figure 16. Dynamic scintigraphic image showing the biodistribution of DTPA-SPION MB as measured in ROIs on dynamic images at 1 h (A) and 24 h (B) post-*i.v.* injection.

4.4   *IN VIVO* IMAGING SYSTEM

MB were mainly distributed to the lungs as seen using IVIS 2D and 3D. At 30 min, 2 h and 4 h post-injection, the fluorescence signal was mainly seen in the lungs and liver, while at 24 h the signal had re-distributed to be seen mainly in the liver. The results obtained from *in vivo* 3D FLIT images were in agreement with those obtained from *ex vivo* 2D fluorescence images of uptake in the organs.

4.5   PHARMACOKINETIC MODELING

MR imaging could be used for calculating and presenting the elimination of SPION MB using a pharmacokinetic model by WinNonLin version 5.0 (Pharsight, Mountain View, CA, USA). The concentration of single layer SPION MB in the liver at the different time points was calculated and represented as µg/mL versus time (h). The maximum concentration (C_{max}) was calculated to be reached after 1.2 h, after which the concentration decreased. The half-life ($T_{1/2}$) was 598.2 ± 97.3 h for SPION MB. $T_{1/2}$ of SPION MB in rat liver was 598.2 ± 97.3 h, while SPION had a half-life in liver of 222.6 ± 26.4 h. Clearance (CL) was 0.011 ± 0.003 mL/h for SPION MB, while for

SPION it was 0.026 ± 0.0027. T_{max} for SPION MB was calculated to be 1.17 ± 0.52 h, while T_{max} for SPION was 0.44 ± 0.15 h. The maximum concentration C_{max} was calculated to be 94.0 ± 13.6 µg for SPION MB, while SPION had a C_{max} of 102.2 ± 2.3 µg. R2* values in other organs such as brain, kidneys and muscle are not shown since calculations of T2* in these organs showed no signal decrease compared to pre-injection.

4.6 THERANOSTICS AND DRUG DELIVERY

4.6.1 Busulfan Labeled Microbubbles

Busulfan was successfully incorporated into MC with a yield of 20 % of the initial drug concentration. Imaging of injected busulfan MC labeled with ^{99m}Tc using SPECT-CT showed that busulfan MCs are distributed mainly to the liver and spleen of the rat.

4.6.2 [99m]Tc Labeled Dexamethasone-DOTA-SPION Microbubbles for the Treatment of Muscle Inflammation in Rat

The T2 TIRM MR sequence can image muscle inflammation. A high signal area was visualized at the place of the injection. This could show the muscle being inflamed due to liquefaction around the inflammation; alternatively, the high signal area of the rat leg might also be caused by remains of the injected lipopolysaccharides (LPS) in liquid form, since fluids produce a bright signal on T2 TIRM images.
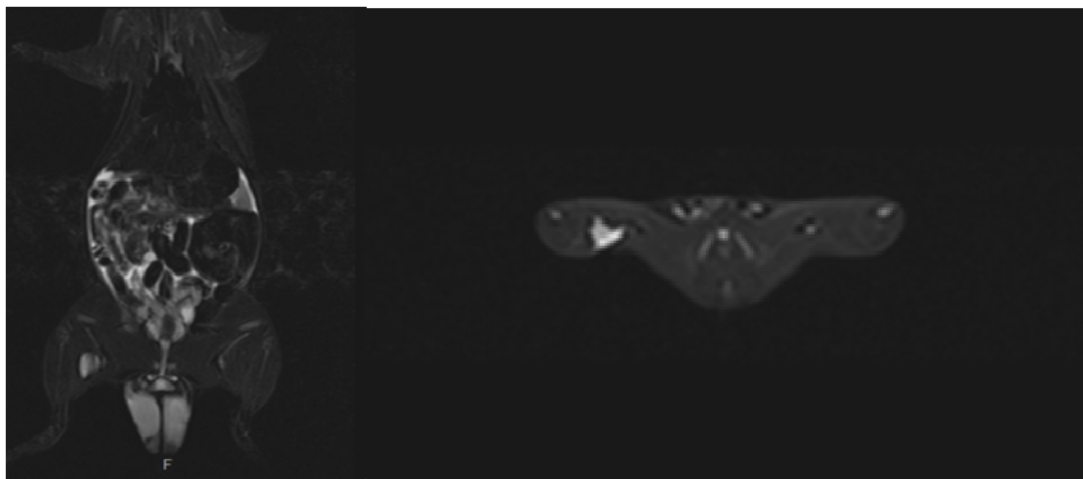
Figure 17. A rat imaged at 3 T MRI (Siemens Trio, Siemens, Erlangen, Germany) using T2 Turbo Inversion Recovery Magnitude (TIRM) in the coronal plane (A) and in the transversal plane (B) after the intra muscular injection of LPS. TE = 80 ms, TR = 5000 ms and flip angle 120.

[99m]Tc Labeled Dexamethasone-DOTA-SPION MB were injected and the radioactivity was measured immediately post-injection by using a Gamma probe. The number of counts measured using the Gamma probe on the legs and respective organs were as follows: in the right hind leg 5000, left hind leg 3000, liver 60 000, lungs 50 000 and intestines 40 000 counts.

36
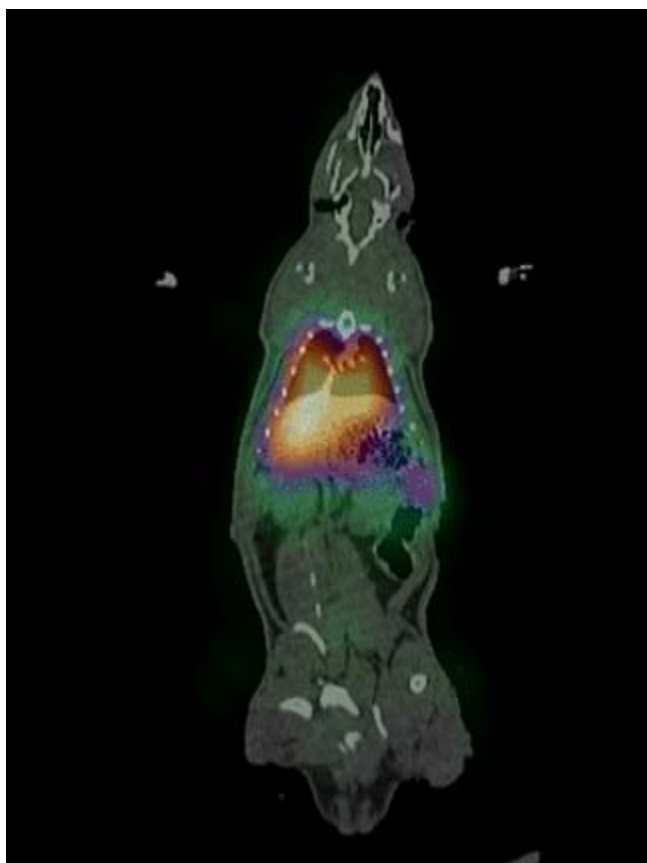
Figure 18. A rat injected with ^{99m}Tc labeled Dexamethasone-DOTA-SPION MB and imaged using fusion SPECT/CT (Siemens T-16). The MB were mainly distributed to the lungs and the liver at 1 h post-injection.

5 DISCUSSION

In this thesis we have shown that ligand functionalized DTPA-, NOTA-, chitosan-, PMAA-, DTPA-SPION-, NOTA-SPION and Dexamethasone-DOTA-SPION MB can be labeled with ^{99m}Tc to enable imaging using nuclear medicine imaging techniques. Different ligands affected the yield of labeling of MBs, however, we have also observed that plain MB could be labeled, which could be explained by the unspecific uptake or incorporation of radiomarkers by the polymer matrix. The highest labeling yield was observed in MB functionalized with DTPA, followed by PMAA and NOTA. The distribution of MB in Sprague Dawley rats was studied using dynamic planar scintigraphy (2D) and SPECT/CT (3D tomography). Hybrid imaging using the combination of SPECT and CT images was performed by fusing images to produce SPECT/CT imaging. SPECT is utilized to show the locations of uptake of radiomarker, while CT gives an anatomical map of the body which will be used for verification of which organs are involved. Hybrid imaging or multimodal imaging is frequently used in clinical practice. The use of multimodal contrast agents such as ligand functionalized MB is an important step towards enabling more effective use of this technique. Attachment of ^{99m}Tc as a ligand for further labeling gives us a dual modality contrast agent (US and SPECT). Moreover, if we then incorporate a CT contrast, we would enable trimodality use. If SPION are also attached to the MB we enable MR imaging, making the agent multimodal.

When rats were injected with the ^{99m}Tc ligand functionalized MB *intravenously* through the tail vein, the contrast agent was mainly distributed to the lungs and to some extent to the liver at 1 h post-injection. After 24 h the distribution had relocated to the liver. Some uptake was shown in the kidney 24 h post-injection, which could probably be due to free ^{99m}Tc being liberated from the MB *in vivo* and eliminated mainly through the kidneys. A possible explanation could also be that the MB polymer matrix partly breaks into small pieces *in vivo*. However, histological examination shows no signs of broken MB in the organs. By applying an *in vitro* test using labeled MB resuspended in saline, we could detect that a non-significant amount of ^{99m}Tc had been released from the MB at 10 min, 30 min, 1, 3 and 24 h after ^{99m}Tc-labeling. Verification of nuclear medicine imaging was carried out by removing the organs and measuring their radioactivity *post mortem*. A hybrid imaging technique merging nuclear medicine images with MRI was examined. The rats were injected with ligand functionalized ^{99m}Tc SPION MB and imaged first by SPECT and subsequently by 3 T MRI. By importing the MR image into the Hermes system, we were able to fuse the images and obtain a SPECT/MR image. The organ location of uptake could be distinguished exactly by this technique since MRI is superior in soft tissue contrast. Since the MB were labeled by SPION, MRI brought another dimension to the imaging result. While SPECT showed the uptake of MB primarily in the lungs, MRI showed uptake in the liver by signal decrease caused by the iron oxide. When studying the organs histologically we could show that as early as 2 h post-injection there was significant findings of MB in the liver. There was a continues decrease of the MR signal during the

first 24 h. To establish the distribution of ^{99m}Tc-labeled MB, a reference containing free ^{99m}Tc pertechnetate was injected into the rat. The distribution was mainly seen in the stomach, kidneys and bladder. Some radioactivity was also observed in the thymus, thyroid gland and mouth mucosal membranes. The different distribution observed after free ^{99m}Tc pertechnetate and ^{99m}Tc labeled MB indicates that no free ^{99m}Tc was present in the solution when injecting ^{99m}Tc-labeled MB. Furthermore, the radioactivity in the respective organs was measured by drawing ROIs on the dynamic scintigraphic images and was found to be in agreement with visual evaluation of the SPECT/CT images. Not only the different ligands but the size, lipophilicity or building of polymer aggregates with a diameter larger than 5 micrometers could potentially cause the MB to be trapped in the capillary bed of the lungs. Aggregates and also large conglomerates of MB were unfortunately seen in the lungs in histology slides. However, after 24 h an accumulation of radioactivity was observed in the liver, which was shown to be MB taken up by macrophages using immunohistochemistry. Macrophage uptake was also visualized in the lungs and spleen. The disadvantage of using clinical equipment for the rats was the lower resolution which made it difficult to study the spleen by multimodal imaging techniques. However, the histology bridges the gap in imaging and verifying organ uptake of MB. The different imaging techniques thus give extra dimensions to the information on biodistribution, elimination, and physiological status that enhances the interpretation of data.

A high labeling yield of DTPA-SPION MB and their application for multimodal imaging SPECT/CT/MRI could favor these MB for further studies as a theranostic candidate for drug delivery of cytostatics and imaging of cancers. Moreover, one could hypothesize that what was found in the liver was ^{99m}Tc-Tin colloids, which have historically been used as a radiopharmaceutical to measure and image liver function. However, Kyung *et al.* injected both pigs and rats with ^{99m}Tc-Tin colloids to follow their biodistribution and concluded that in small animals (rats) the ^{99m}Tc-Tin colloids distributed exclusively to the liver directly post-injection [91, 92]. In our study we observed the distribution to the lungs within the first hour, which indicates that our labeled MB did not contain colloids. Most of the colloids were probably removed from the MB through the washing steps.

In the present thesis, MR imaging was furthermore used as a new method to determine the pharmacokinetic parameters and the biodistribution of SPION MB in the rat by measuring the R2* relaxivity caused by SPION MB on T2* weighted images and correlating R2* with iron oxide concentration using a standard curve obtained from phantom imaging of SPION MB. The calculated concentration of SPION MB at different time points could furthermore determine their elimination.

Yang *et al.* [93] have studied another type of microbubble, PLA-PVA (poly (DL-lactide)-polyvinyl alcohol) double-layered microbubbles with Fe_3O_4-inclusion. The authors found that the transverse relaxation rate (R2*) increases more rapidly the greater the volume. According to Yang, inclusion of SPION into the microbubbles enhances the contrast obtained both by MR and ultrasound imaging. Cai et al [94] have

further shown that when using the appropriate ultrasound exposure to SPION microbubbles aimed for MR imaging, the nanoparticles can be released to the desired organ of interest when the microbubbles collapse due to exposure to ultrasound.

Weissleder *et al.* [95] have administered radio-labeled AMI-25 (59Fe AMI-25) at a dose of 40-50 µmol to the rat. The authors fitted the blood concentration data to a one-compartment elimination model and reported the half-life in the blood to be six minutes, while the clearance from the liver occurred with a half-life of three days and from the spleen with a half-life of four days. This half-life was much shorter than the one in the present study; however, the authors measured half life in blood while we have measured it in liver tissue.

Majumdar *et al.* [96] have described the elimination of iron containing AMI25 by a biphasic elimination model. Majumdar *et al.* calculated alpha half-life to 10 minutes while beta half-life was calculated to be approximately 92 minutes and about 60 % was taken up in the liver. These results may reflect the rapid clearance of the blood circulation and indicate that the iron nanoparticles were accumulated in the liver, which was also observed in the present investigation.

Iron compounds such as AMI-25 were shown to be phagocytized by healthy liver Kupffer cells but not by hepatocellular carcinomas (HCCs); since they do not have phagocytizing capability. These results in hepatocellular carcinomas that were appearing bright on T2 and T2* weighted MR images while the healthy liver and spleen containing phagocytized SPION appeared dark [97]. In some of our rats we could detect white areas in the liver, indicating that those rats might have cysts or tumors which appear bright on the T2* weighted images. However, this should be further investigated. In patients with liver metastases [98], the blood clearance of AMI has been described by a two-compartment model with an alpha-elimination phase of 4.4 - 22.2 minutes. The beta-elimination half-life ranged from 79 to 309 minutes. This short half-life may also indicate the rapid clearance from the blood and accumulation in the liver.

Coating of SPION or SPION MB with different biocompatible polymers could change their half-life and facilitate their uptake. Xiao *et al.* have shown that the blood half-life was prolonged from 40 minutes to 120 minutes when zwitterionic coated SPION were compared with poly (acrylic) acid coated SPION, respectively [80]. However, no half-life in liver tissue was reported. Moore *et al.* [99] showed that the uptake of dextran-coated SPION was 10 fold higher in brain tumors compared to healthy brain tissue. The authors reported a 3-4.5 h plasma half-life of SPION in rodents, while the peak concentration was reached in tumor tissues 24 h post-injection. Stephen *et al.* [100] have shown that hydrophobic coating of the SPION, such as PEG or a zwitterionic coating, could make the SPION avoid RES uptake and thereby stay longer in the circulation. In our study, SPION were uncoated and therefore most probably cleared rapidly from the circulation and accumulated in the liver, where they were eliminated slowly.

SPION have been suggested as a targeting contrast agent for cancer imaging and diagnostics [81]. Since tumors have little lymphatic drainage, retained SPION in the tumor tissue should increase the contrast between tumor tissue containing SPION and healthy tissue, provided that the healthy tissue has no active uptake of SPION.
In this thesis we have applied dynamic imaging using the T2* sequence.

Briley-Saebo studied different coating materials and their effect on iron oxide particles *in vivo* and found that coating decreased the half-life of the particles [101]. The authors reported that the half-life of iron oxide particles in rat liver was 8 days for dextran coated materials, 10 days for carboxy dextran coated materials, 14 days for unformulated oxidized starch and 29 days for formulated oxidized starch. In the present studies we observed a slightly longer half-life of 31 days for multiple layer PVA SPION MB and 25 days for single layer MB.

In our investigation, SPION and SPION PVA MB were accumulated in the liver quite shortly after administration as measured by using SPECT and MRI. Employing histopathology, we have found that SPION MB are taken up by macrophages in the liver and spleen [90]. SPION MB and SPION did not cause any measurable MR signal decrease in any other organs or tissues including the brain than liver and spleen, indicating that they are rapidly taken up and do not pass the blood brain barrier.
Despite these observations we did not observe negative effects on the liver or spleen such as enlargement or volume reduction due to cirrhosis. This confirms the results by Bacon *et al.* [102], who injected large amounts of ferrite particles and did not observe any hepatotoxic effects or organelle dysfunction. They also observed a clearance from the body within three months. In the work of Yang *et al.* [93] dual polymer PVA-lactic acid microbubbles containing SPION were injected into rats. A maximum signal decrease could be seen approximately 60 min post-injection. However, they did not follow the rats over time to see the return of the signal to base value. Thus no half-life was calculated in their study.

Furthermore, we have investigated how repeated application of the 3 T magnetic field might affect MB wall integrity and accelerate iron loss to the tissues. Our studies did not show any histological indication for increased tissue iron load. The initially widespread intravascular clustering of SPION MB that was seen in the lungs mainly resolved after three weeks. An indication for possible adverse effects of *intravenous* administration of large numbers of SPION MB was found in the lungs of two rats at later time points, where we observed remains of organized vascular thrombi and focal granulomas.

Theranostic experiments were carried out by loading MC with the cytostatic drug Busulfan. Busulfan incorporation into MC showed a good yield that should be sufficient for clinical use. Imaging using SPECT/CT can be utilized to visualize the dynamic bio-distribution of the cytostatic loaded MB and MCs in order to confirm uptake in the target organ. Incorporating the drug into capsules that are specifically accumulated in the target organ might enable dose reduction and hence decrease side

effects. The combination of treatment and diagnostics by imaging, theranostics, could be successful for the early detection of disease, imaging the progression of disease progression treatment effect.

The theranostic experiments carried out concerning imaging and treatment of muscle inflammation are in an initial phase [103, 104]. Muscle inflammation caused by an intramuscular injection could be successfully imaged using the T2 TIRM MR sequence. Uptake of targeted ^{99m}Tc labeled Dexamethasone-DOTA-SPION MB could moreover be imaged using SPECT/CT or SPECT/MRI and uptake of ^{99m}Tc labeled MB in a specific, small region could be measured using a gamma probe. However since the distribution of the investigated MB were mainly to the lungs and liver, treatment of muscle inflammation was not obtained at this stage. We can speculate that by changing the size of MB and/or by applying a coating to MB could make them avoid RES uptake and thus be drawn to the magnet attached by the muscle for a potential treatment of inflammation.

6 CONCLUSIONS

In conclusion, MB functionalized by different ligands can be labeled with radiotracers and utilized for SPECT/CT, while the incorporation of SPION in or between the MB shells enables imaging using MR, hence enabling combined multimodal SPECT/MR imaging. Our investigation revealed that the biodistribution may be modified using different ligands. Furthermore, using a single contrast agent with multimodal imaging, fusion SPECT/CT followed by MRI enables visualization of functional and anatomical information in one image, thus improving the diagnostic benefit to patients. Our results showed SPION MB to be a good contrast candidate for MR imaging. Moreover, MRI is a reliable and non-invasive tool that can be utilized to study the pharmacokinetics of SPION MB and SPION.

The current studies characterized the properties of SPION MB in terms of size, size distribution, the effect on rat tissue in various organs *in vivo*, distribution, biological fate and relaxivity using MRI. The histological findings were in good agreement with the findings from MR imaging.

Furthermore, we have shown that SPION PVA MB act as good contrast agent for the liver, which could be advantageous for diagnostics, including cancer diagnostics. We have also shown that sham vehicles such as plain MB without SPION give no more contrast compared to blank liver tissue on T2* weighted images. However, the SPION PVA MB were eliminated from the liver with a long half-life, which probably is not desirable in all clinical settings but could be advantageous for cancer imaging of the liver. MB have been labeled using Alexa-680 Vivo Tag, which enabled the use of *in vivo* imaging system (IVIS) and ultrasound for biodistribution studies as well as fluorescence microscopy for histological verification. Several studies are ongoing to modify SPION PVA MB in order to optimize their kinetics and use in clinical studies.

7 FUTURE ASPECTS

Further investigations should address the dynamics of drug release from the MB, modifications for organ targeting, size effect on biodistribution and kinetics, tendency to cluster *in vivo*, and delivery dynamics during administration to attenuate possible adverse effects on the pulmonary vasculature. Future studies should address the toxicity of MB *in vivo*, and targeting of MB should be investigated to illustrate the binding to diseased organs. Furthermore, the loading of MB with drugs could employ them as a theranostic vehicle for treatment. Coating the MB with PEG could, moreover, change their biodistribution and elimination. The current distribution of MB to the liver could make them usable for the detection of cancerous disease in the liver. Distribution to the pancreas should be investigated. As a conclusion, more preclinical studies are warranted before taking MB to a clinical setting. The characteristics of the polymer matrix enabling it to be coupled to ligands and drugs, as well as the ability to attach imaging markers to it, make the future possibilities of MB unlimited.

8 ACKNOWLEDGEMENTS

9 REFERENCES

1.	Semelka, R.C. and T.K. Helmberger, *Contrast agents for MR imaging of the liver.* Radiology, 2001. 218(1): p. 27-38.
2.	Babos, M., et al., *In vitro evaluation of alternative oral contrast agents for MRI of the gastrointestinal tract.* European Journal of Radiology, 2008. 65(1): p. 133-139.
3.	Maravilla, K.R., et al., *Contrast enhancement of central nervous system lesions: Multicenter intraindividual crossover comparative study of two MR contrast agents.* Radiology, 2006. 240(2): p. 389-400.
4.	Lin, Y., Z.Y. Chen, and F. Yang, *Ultrasound-based multimodal molecular imaging and functional ultrasound contrast agents.* Curr Pharm Des, 2013. 19(18): p. 3342-51.
5.	Mitchell, N., et al., *Incorporation of paramagnetic, fluorescent and PET/SPECT contrast agents into liposomes for multimodal imaging.* Biomaterials, 2013. 34(4): p. 1179-92.
6.	John, R., et al., *Targeted multifunctional multimodal protein-shell microspheres as cancer imaging contrast agents.* Mol Imaging Biol, 2012. 14(1): p. 17-24.
7.	Sharma, P., et al., *Multimodal nanoparticulate bioimaging contrast agents.* Methods Mol Biol, 2010. 624: p. 67-81.
8.	Frullano, L. and T.J. Meade, *Multimodal MRI contrast agents.* J Biol Inorg Chem, 2007. 12(7): p. 939-49.
9.	Oostendorp, M., et al., *Pharmacokinetics of contrast agents targeted to the tumor vasculature in molecular magnetic resonance imaging.* Contrast Media Mol Imaging, 2010. 5(1): p. 9-17.
10.	Lawaczeck, R., G. Jost, and H. Pietsch, *Pharmacokinetics of contrast media in humans: model with circulation, distribution, and renal excretion.* Invest Radiol, 2011. 46(9): p. 576-85.
11.	Schuhmann-Giampieri, G., *Liver contrast media for magnetic resonance imaging. Interrelations between pharmacokinetics and imaging.* Invest Radiol, 1993. 28(8): p. 753-61.
12.	Eloy, R., C. Corot, and J. Belleville, *Contrast media for angiography: physicochemical properties, pharmacokinetics and biocompatibility.* Clin Mater, 1991. 7(2): p. 89-197.
13.	Saari, A., *Pharmacokinetics of three contrast media in experimental pancreatography.* Acta Radiol, 1989. 30(1): p. 81-6.
14.	Jensen, L.I., et al., *Contrast media for CT. An analysis of the early pharmacokinetics.* Invest Radiol, 1985. 20(8): p. 867-70.
15.	Gardeur, D., et al., *Pharmacokinetics of contrast media: experimental results in dog and man with CT implications.* J Comput Assist Tomogr, 1980. 4(2): p. 178-85.
16.	Engelen, A.J., J.F. Rodrigues De Maranda, and E.J. Ariens, *Pharmacokinetics of renal contrast media. I. Renal excretion processes studied in dogs by the stop-flow technique.* Invest Radiol, 1973. 8(4): p. 210-8.
17.	Cavalieri, F., et al., *Tethering functional ligands onto shell of ultrasound active polymeric microbubbles.* Biomacromolecules, 2006. 7(2): p. 604-611.
18.	Barrefelt, A.A., et al., *Multimodality imaging using SPECT/CT and MRI and ligand functionalized 99mTc-labeled magnetic microbubbles.* EJNMMI Res, 2013. 3(1): p. 12.

19. Smolensky, E.D., et al., *Scaling laws at the nanosize: the effect of particle size and shape on the magnetism and relaxivity of iron oxide nanoparticle contrast agents.* Journal of Materials Chemistry B, 2013. 1(22): p. 2818-2828.

20. Barrefelt, A., et al., *Biodistribution, kinetics, and biological fate of SPION microbubbles in the rat.* International Journal of Nanomedicine, 2013. 8: p. 3241-3254.

21. Brismar, T.B., et al., *Magnetite Nanoparticles Can Be Coupled to Microbubbles to Support Multimodal Imaging.* Biomacromolecules, 2012. 13(5): p. 1390-1399.

22. Swindle, M.M., A.C. Smith, and B.J. Hepburn, *Swine as models in experimental surgery.* J Invest Surg, 1988. 1(1): p. 65-79.

23. Ustuner, E.T., et al., *Swine composite tissue allotransplant model for preclinical hand transplant studies.* Microsurgery, 2000. 20(8): p. 400-6.

24. Shigeta, T., et al., *Transgenic pig expressing the red fluorescent protein kusabira-orange as a novel tool for preclinical studies on hepatocyte transplantation.* Transplant Proc, 2013. 45(5): p. 1808-10.

25. Thim, T., et al., *Familial hypercholesterolaemic downsized pig with human-like coronary atherosclerosis: a model for preclinical studies.* EuroIntervention, 2010. 6(2): p. 261-8.

26. Jewel, K.L., et al., *Imaging: magnetic resonance imaging (MRI).* J Med Soc N J, 1984. 81(10): p. 884-8.

27. Damadian, R., *Field focusing n.m.r. (FONAR) and the formation of chemical images in man.* Philos Trans R Soc Lond B Biol Sci, 1980. 289(1037): p. 489-500.

28. Damadian, R., et al., *Human tumors detected by nuclear magnetic resonance.* Proc Natl Acad Sci U S A, 1974. 71(4): p. 1471-3.

29. Damadian, R., L. Minkoff, and M. Goldsmith, *Whole-body nuclear magnetic resonance scanning: n.m.r. studies of tumour cells.* Ciba Found Symp, 1978(67): p. 131-41.

30. Lauterbur, P.C., *NMR imaging in biomedicine.* Cell Biophys, 1986. 9(1-2): p. 211-4.

31. Lauterbur, P.C., *Cancer detection by nuclear magnetic resonance zeugmatographic imaging.* Cancer, 1986. 57(10): p. 1899-904.

32. Lauterbur, P.C., *Progress in n.m.r. zeugmatography imaging.* Philos Trans R Soc Lond B Biol Sci, 1980. 289(1037): p. 483-7.

33. Drost, D.J., et al., *Proton magnetic resonance spectroscopy in the brain: report of AAPM MR Task Group #9.* Med Phys, 2002. 29(9): p. 2177-97.

34. Chavhan, G.B., et al., *Principles, techniques, and applications of T2*-based MR imaging and its special applications.* Radiographics, 2009. 29(5): p. 1433-49.

35. Karaus, A., et al., *Black-blood imaging of the human heart using rapid stimulated echo acquisition mode (STEAM) MRI.* Journal of Magnetic Resonance Imaging, 2007. 26(6): p. 1666-1671.

36. Reed, A.B., *The history of radiation use in medicine.* J Vasc Surg, 2011. 53(1 Suppl): p. 3S-5S.

37. Kojima, C., et al., *X-ray computed tomography contrast agents prepared by seeded growth of gold nanoparticles in PEGylated dendrimer.* Nanotechnology, 2010. 21(24): p. 245104.

38. Hutton, B.F., *The origins of SPECT and SPECT/CT.* Eur J Nucl Med Mol Imaging, 2013.

39. Tapscott, E., *First scintillation camera is foundation for modern imaging systems.* Journal of Nuclear Medicine, 1998. 39(3): p. 15N-+.

40. Tapscott, E., *Nuclear medicine pioneer: Hal O. Anger. First scintillation camera is foundation for modern imaging systems.* J Nucl Med, 1998. 39(3): p. 15N, 19N, 26N-27N.

41. Cai, J. and F. Li, *Single-photon emission computed tomography tracers for predicting and monitoring cancer therapy.* Curr Pharm Biotechnol, 2013. 14(7): p. 693-707.

42. Hamamura, M.J., et al., *Development of an MR-compatible SPECT system (MRSPECT) for simultaneous data acquisition.* Phys Med Biol, 2010. 55(6): p. 1563-75.

43. Misri, R., K. Saatchi, and U.O. Hafeli, *Nanoprobes for hybrid SPECT/MR molecular imaging.* Nanomedicine (Lond), 2012. 7(5): p. 719-33.

44. Toubert, M.E., et al., *Additional Diagnostic Value of Hybrid SPECT-CT Systems Imaging in Patients With Differentiated Thyroid Cancer.* Am J Clin Oncol, 2012.

45. Vasquez, K.O., C. Casavant, and J.D. Peterson, *Quantitative whole body biodistribution of fluorescent-labeled agents by non-invasive tomographic imaging.* PLoS One, 2011. 6(6): p. e20594.

46. Blanc, F., et al., *99mTc ovalbumin labelled eggs for gastric emptying scintigraphy: in-vitro comparison of solid food markers.* Nucl Med Commun, 2005. 26(11): p. 1021-5.

47. Rollin-Sillaire, A., et al., *Contribution of single photon emission computed tomography to the differential diagnosis of dementia in a memory clinic.* J Alzheimers Dis, 2012. 30(4): p. 833-45.

48. Miziara, J.M., et al., *Preoperative nodal staging of non-small cell lung cancer using 99mTc-sestamibi spect/ct imaging.* Clinics (Sao Paulo), 2011. 66(11): p. 1901-9.

49. Glaudemans, A.W., et al., *Bone scintigraphy with technetium-hydroxymethylene diphosphonate allows early diagnosis of cardiac involvement in patients with transthyretin-derived systemic amyloidosis.* Amyloid, 2014.

50. Greenwood, J.P., et al., *Comparison of Cardiovascular Magnetic Resonance and Single-Photon Emission Computed Tomography in Women with Suspected Coronary Artery Disease from the CE-MARC Trial.* Circulation, 2013.

51. Ortiz-Arzate, Z., et al., *Kit preparation and biokinetics in women of 99mTc-EDDA/HYNIC-E-[c(RGDfK)]2 for breast cancer imaging.* Nucl Med Commun, 2013.

52. Madru, R., et al., *99mTc-labeled superparamagnetic iron oxide nanoparticles for multimodality SPECT/MRI of sentinel lymph nodes.* J Nucl Med, 2012. 53(3): p. 459-63.

53. Silva, W.E., et al., *New homotrinuclear lanthanide complexes: synthesis, characterization and spectroscopic study.* J Phys Chem A, 2010. 114(37): p. 10066-75.

54. Liang, M., et al., *Multimodality Nuclear and Fluorescence Tumor Imaging in Mice Using a Streptavidin Nanoparticle.* Bioconjugate Chemistry, 2010. 21(7): p. 1385-1388.

55. Baselga, J., et al., *Lapatinib with trastuzumab for HER2-positive early breast cancer (NeoALTTO): a randomised, open-label, multicentre, phase 3 trial.* Lancet, 2012. 379(9816): p. 633-40.

56. Rijcken, E., et al., *ICAM-1 and VCAM-1 antisense oligonucleotides attenuate in vivo leucocyte adherence and inflammation in rat inflammatory bowel disease.* Gut, 2002. 51(4): p. 529-35.

57. Hua, S., *Targeting sites of inflammation: intercellular adhesion molecule-1 as a target for novel inflammatory therapies.* Front Pharmacol, 2013. 4: p. 127.

58. Krasia-Christoforou, T. and T.K. Georgiou, *Polymeric theranostics: using polymer-based systems for simultaneous imaging and therapy.* Journal of Materials Chemistry B, 2013. 1(24): p. 3002-3025.

59. Singh, R.K., et al., *Multifunctional hybrid nanocarrier: Magnetic CNTs ensheathed with mesoporous silica for drug delivery and imaging system.* ACS Appl Mater Interfaces, 2014.

60. Li, S., et al., *Novel Multifunctional Theranostic Liposome Drug Delivery System: Construction, Characterization, and Multimodality MR, Near-Infrared Fluorescent, and Nuclear Imaging.* Bioconjug Chem, 2012.

61. Chen, H.H., et al., *MR imaging of biodegradable polymeric microparticles: a potential method of monitoring local drug delivery.* Magn Reson Med, 2005. 53(3): p. 614-20.

62. de Smet, M., et al., *SPECT/CT imaging of temperature-sensitive liposomes for MR-image guided drug delivery with high intensity focused ultrasound.* J Control Release, 2013. 169(1-2): p. 82-90.

63. Li, W.M., S.Y. Chen, and D.M. Liu, *In situ doxorubicin-CaP shell formation on amphiphilic gelatin-iron oxide core as a multifunctional drug delivery system with improved cytocompatibility, pH-responsive drug release and MR imaging.* Acta Biomater, 2013. 9(2): p. 5360-8.

64. Shi, J., et al., *PEGylated fullerene/iron oxide nanocomposites for photodynamic therapy, targeted drug delivery and MR imaging.* Biomaterials, 2013. 34(37): p. 9666-77.

65. Sun, C., J.S. Lee, and M. Zhang, *Magnetic nanoparticles in MR imaging and drug delivery.* Adv Drug Deliv Rev, 2008. 60(11): p. 1252-65.

66. Yang, X., et al., *Multifunctional stable and pH-responsive polymer vesicles formed by heterofunctional triblock copolymer for targeted anticancer drug delivery and ultrasensitive MR imaging.* ACS Nano, 2010. 4(11): p. 6805-17.

67. Zhang, L., et al., *Multifunctional and degradable zwitterionic nanogels for targeted delivery, enhanced MR imaging, reduction-sensitive drug release, and renal clearance.* Biomaterials, 2011. 32(20): p. 4604-8.

68. Zhu, L., et al., *Multifunctional pH-sensitive superparamagnetic iron-oxide nanocomposites for targeted drug delivery and MR imaging.* J Control Release, 2013. 169(3): p. 228-38.

69. Butoescu, N., et al., *Dexamethasone-containing biodegradable superparamagnetic microparticles for intra-articular administration: physicochemical and magnetic properties, in vitro and in vivo drug release.* Eur J Pharm Biopharm, 2009. 72(3): p. 529-38.

70. Butoescu, N., et al., *Dexamethasone-containing PLGA superparamagnetic microparticles as carriers for the local treatment of arthritis.* Biomaterials, 2009. 30(9): p. 1772-80.

71. Hall, A.P., et al., *Comparison of computerized image analysis with traditional semiquantitative scoring of Perls' Prussian Blue stained hepatic iron deposition.* Toxicol Pathol, 2013. 41(7): p. 992-1000.

72. Sprague, W.S., et al., *Hemochromatosis secondary to repeated blood transfusions in a dog.* Vet Pathol, 2003. 40(3): p. 334-7.

73. Grishenkov, D., et al., *Characterization of Acoustic Properties of Pva-Shelled Ultrasound Contrast Agents: Ultrasound-Induced Fracture (Part Ii).* Ultrasound in Medicine and Biology, 2009. 35(7): p. 1139-1147.

74. Otani, K. and K. Yamahara, *Development of antibody-carrying microbubbles based on clinically available ultrasound contrast agent for targeted molecular imaging: a preliminary chemical study.* Mol Imaging Biol, 2011. 13(2): p. 250-6.

75.   Kiessling, F., et al., *Ultrasound microbubbles for molecular diagnosis, therapy, and theranostics.* J Nucl Med, 2012. 53(3): p. 345-8.

76.   Dutta, R.K. and S. Sahu, *Development of a novel probe sonication assisted enhanced loading of 5-FU in SPION encapsulated pectin nanocarriers for magnetic targeted drug delivery system.* Eur J Pharm Biopharm, 2012. 82(1): p. 58-65.

77.   Singh, N., et al., *Potential toxicity of superparamagnetic iron oxide nanoparticles (SPION).* Nano Rev, 2010. 1.

78.   Yu, M.K., et al., *Drug-loaded superparamagnetic iron oxide nanoparticles for combined cancer imaging and therapy in vivo.* Angew Chem Int Ed Engl, 2008. 47(29): p. 5362-5.

79.   Mudshinge, S.R., et al., *Nanoparticles: Emerging carriers for drug delivery.* Saudi Pharmaceutical Journal, 2011. 19(3): p. 129-141.

80.   Xiao, W., et al., *Prolonged in vivo circulation time by zwitterionic modification of magnetite nanoparticles for blood pool contrast agents.* Contrast Media Mol Imaging, 2012. 7(3): p. 320-7.

81.   Rosen, J.E., et al., *Iron oxide nanoparticles for targeted cancer imaging and diagnostics.* Nanomedicine, 2012. 8(3): p. 275-90.

82.   El-Dakdouki, M.H., et al., *Development of multifunctional hyaluronan-coated nanoparticles for imaging and drug delivery to cancer cells.* Biomacromolecules, 2012. 13(4): p. 1144-51.

83.   Ernsting, M.J., et al., *Tumor-targeted drug delivery using MR-contrasted docetaxel - carboxymethylcellulose nanoparticles.* Biomaterials, 2012. 33(15): p. 3931-41.

84.   Cavalieri, F., et al., *Stable polymeric microballoons as multifunctional device for biomedical uses: Synthesis and characterization.* Langmuir, 2005. 21(19): p. 8758-8764.

85.   Brismar, T.B., et al., *Magnetite nanoparticles can be coupled to microbubbles to support multimodal imaging.* Biomacromolecules, 2012. 13(5): p. 1390-9.

86.   Peyratout, C.S. and L. Dahne, *Tailor-made polyelectrolyte microcapsules: from multilayers to smart containers.* Angew Chem Int Ed Engl, 2004. 43(29): p. 3762-83.

87.   Morawietz, G., et al., *Revised guides for organ sampling and trimming in rats and mice--Part 3. A joint publication of the RITA and NACAD groups.* Exp Toxicol Pathol, 2004. 55(6): p. 433-49.

88.   Kittel, B., et al., *Revised guides for organ sampling and trimming in rats and mice--Part 2. A joint publication of the RITA and NACAD groups.* Exp Toxicol Pathol, 2004. 55(6): p. 413-31.

89.   Ruehl-Fehlert, C., et al., *Revised guides for organ sampling and trimming in rats and mice--part 1.* Exp Toxicol Pathol, 2003. 55(2-3): p. 91-106.

90.   Barrefelt, A., et al., *Biodistribution, kinetics, and biological fate of SPION microbubbles in the rat.* Int J Nanomedicine, 2013. 8: p. 3241-54.

91.   Shim, K.M., et al., *A Detailed Examination of Pulmonary Uptake of (99m)Tc-Tin Colloid in Healthy Mature Miniature Pigs.* In Vivo, 2009. 23(4): p. 551-554.

92.   *[The European pharmacopeia].* Fortschr Med, 1980. 98(4): p. (150).

93.   Yang, F., et al., *Superparamagnetic iron oxide nanoparticle-embedded encapsulated microbubbles as dual contrast agents of magnetic resonance and ultrasound imaging.* Biomaterials, 2009. 30(23-24): p. 3882-3890.

94.   Cai, X., F. Yang, and N. Gu, *Applications of magnetic microbubbles for theranostics.* Theranostics, 2012. 2: p. 103-12.

95. Weissleder, R., et al., *Superparamagnetic iron oxide: pharmacokinetics and toxicity.* AJR Am J Roentgenol, 1989. 152(1): p. 167-73.

96. Majumdar, S., S.S. Zoghbi, and J.C. Gore, *Pharmacokinetics of superparamagnetic iron-oxide MR contrast agents in the rat.* Invest Radiol, 1990. 25(7): p. 771-7.

97. Yoshikawa, K., et al., *[Clinical application of AMI-25 (superparamagnetic iron oxide) for the MR imaging of hepatic tumors: a multicenter clinical phase III study].* Nihon Igaku Hoshasen Gakkai Zasshi, 1994. 54(2): p. 137-53.

98. Stark, D.D., et al., *Superparamagnetic iron oxide: clinical application as a contrast agent for MR imaging of the liver.* Radiology, 1988. 168(2): p. 297-301.

99. Moore, A., et al., *Tumoral distribution of long-circulating dextran-coated iron oxide nanoparticles in a rodent model.* Radiology, 2000. 214(2): p. 568-74.

100. Stephen, Z.R., F.M. Kievit, and M. Zhang, *Magnetite Nanoparticles for Medical MR Imaging.* Mater Today (Kidlington), 2011. 14(7-8): p. 330-338.

101. Briley-Saebo, K.C., et al., *Clearance of iron oxide particles in rat liver: effect of hydrated particle size and coating material on liver metabolism.* Invest Radiol, 2006. 41(7): p. 560-71.

102. Bacon, B.R., et al., *Ferrite particles: a new magnetic resonance imaging contrast agent. Lack of acute or chronic hepatotoxicity after intravenous administration.* J Lab Clin Med, 1987. 110(2): p. 164-71.

103. Olesen, J., et al., *Skeletal muscle PGC-1alpha is required for maintaining an acute LPS-induced TNFalpha response.* PLoS One, 2012. 7(2): p. e32222.

104. Roth, J., et al., *Attenuation of fever and release of cytokines after repeated injections of lipopolysaccharide in guinea-pigs.* J Physiol, 1994. 477 (Pt 1): p. 177-85.